Biowaste-derived carbon black applied to polyaniline-based high-performance supercapacitor microelectrodes: Sustainable materials for renewable energy applications

Sumita Goswami[a]

Gowra Raghupathy Dillip[b]

Suman Nandy[a, *]

s.nandy@fct.unl.pt, snandy_ju@yahoo.co.in

Arghya Narayan Banerjee[b, **]

arghya@ynu.ac.kr

Ana Pimentel[a]

Sang Woo Joo[b]

Rodrigo Martins[a]

Elvira Fortunato[a, ***]

emf@fct.unl.pt

[a]i3N/CENIMAT, Department of Materials Science, Faculty of Science and Technology, Universidade NOVA de Lisboa and CEMOP/UNINOVA, Campus de Caparica, 2829-516, Caparica, Portugal

[b]School of Mechanical Engineering, Yeungnam University, Gyeongsan, 712-749, South Korea

*Corresponding author.

**Corresponding author.

***Corresponding author.

Abstract

Biowaste, derived from cooking-oven-produced carbon nanoparticles (WCP), are incorporated into polyaniline (PANI) via in-situ chemical oxidative polymerization to achieve excellent electrochemical properties for application in supercapacitors. The WCP-PANI composite electrodes have shown high-performance charge storage, due to combinatorial effect of electrical double layer capacitance from WCP and pseudocapacitance from PANI. With increase in the WCP percolation, work function of PANI is increased, which improves the charge-trapping capabilities of composites. For such distinct charge-trapping mechanism, areal capacitance of the composite microelectrode remains near-constant with increase in scan rate or current density. This indicates the suppression of diffusion limitations at higher scan rates to considerably enhance the rate capability. Also, with increasing polymerization time, strong interaction in this conjugated system greatly improves the charge-transfer reaction between PANI and WCP. The areal capacitance of the composite electrode is found to increase more than 600 times over pure PANI electrode. Moreover, energy-power performance of the microelectrode reveals almost 550% increment in the power density with a mere 1% decrement in energy density. Such rationally synthesized WCP-PANI composite electrodes using biowaste carbon nanomaterials, provide opportunities for the development of next-generation green-supercapacitors with improved energy storage performance.

Keywords: Carbon materials; Biowastes; Polyaniline; Supercapacitors; Sustainable materials

1 Introduction

In recent years, there has been burgeoning interest in waste management systems as the concept of sustainable development has been and still is a subject to criticism. Reduce, reuse and recycle are three basic building

factors in this regard which can accelerate the transformation towards sustainable development goals and post fossil-carbon society. Specially, when the bulk of the world's energy system involve carbon based materials (both as raw and product), recycling of waste carbon to energy materials is an excellent approach to meet the global challenge as well as provide opportunities for waste handling: sustainable materials for renewable energy applications.

On the other hand, to attain the increasing power demands of energy storage systems, particularly of portable electronic devices and the emergent internet-of-things (IoT), both researchers and developers are depending nowadays on “Supercapacitors” [1–4] as a promising alternative approach. Evidently, for this typical interest in supercapacitors, comprehensive research has been endeavored in designing new electrode materials for enhancing the power and energy storage capacity associated to the electrodes [5–10]. Various porous forms of carbon are presently preferred as the electrode materials due to exceptionally high surface areas, comparatively high electronic conductivity, and feasible cost [11,12]. Additionally, other forms of nanostructured carbon-based electrochemical electrodes have also generated considerable interests due to their unique surface structures, high surface-to-volume ratios, and size-dependent physical/chemical properties *etc.*, all of which have led these active materials into higher utilization for superior electrochemical performance [13,14].

But one related issue for the carbon nanomaterials’-based electrochemical devices is the intrinsic grain-boundary scattering of charge carries to deteriorate the transport properties, which affects the electrochemical performance considerably. To overcome this, composite/hybrid electrodes, based on carbon nanomaterials embedded within a conducting polymer layer are fabricated to get improved electrochemical properties. Notably, conducting polymers having properties like good electrical conductivity and high pseudocapacitance, have also emerged widely as interesting electrode material for supercapacitors [8,9,15–17]. Among such conductive polymers, polyaniline (PANI) has been aroused as the most promising one because of its excellent energy storage capacity, low-cost monomer, ease of synthesis and manipulation, interesting doping chemistry, good environmental stability, high conductivity/electro-activity *etc.* [16–19]. The intriguing feature of π-electron delocalization at the backbone of this conjugate polymer can further unfold a distinct charge transfer mechanism by indulging the percolation of carbon nanoparticles (CNPs). Subsequently, this kind of unique combination of two different types of materials would be able to expand the class of novel composite materials, simply controlling their properties through rational chemical synthesis. Researchers therefore have made the hybridization of these two materials (carbon nanomaterials within conducting polymer matrix) to get improvedsynergetic effect in storage capacity by virtue of the combinatorial effect of electric double layer capacitance of carbon nanomaterials and faradic pseudocapacitance of PANI. Additionally, the stability of PANI is also increased by using the carbon support, which considerably increases the cyclability as well as the capacitive performance of the PANI matrix by reducing the swelling and shrinkage of the polymer backbone during charge-discharge. Hence, the power and energy-storage capabilities of these composite devices are extensively related with both physical and chemical characteristics of these hybrid electrodes.

Variety of carbon-based materials within PANI have been explored so far to achieve the envisaged supercapacitor effect, such as activated carbon, mesoporous carbon, carbon aerogel, hollow carbon spheres, nano-diamond, calcium carbide derived carbon, carbon black or even carbon nanotubes (CNT) [20]. Majority of the syntheses processes of these composites have involved either chemical or electrochemical routes, whereas electrochemical characterizations have been performed with two or three electrode cell configurations. However, most of these fabrication methods have used relatively costly, complex and scarcely available feedstocks. Recently, with increasing research interest in sustainable materials from the viewpoint of environmental and cost-effective concerns, the source of component carbon material in this type of supercapacitors are being replaced with renewable feedstocks, having abundant porous structures as well as cheap, easy syntheses processes. These renewable feedstocks are either derived from the abundant and renewable biomass resources (like wood, bamboo, waste tea *etc.*) or extracted from food wastage [21–25] (in the form of porous carbon). But all of these processes reported till date, include some time-consuming and (sometimes) complex pre-treatments or modification procedures for as-derived carbon materials, which again involve some resources and chemicals (especially strong acids), that are costly and can affect the properties of the materials.

In the current report, we have presented for the first time (to the best of the authors’ knowledge), the usage of normal cooking oven-produced waste carbon (that is basically biowaste) within the PANI matrix, without performing any such chemical modifications, for further implicating in PANI-based composite electrochemical electrodes; yet the as-synthesized composite microelectrodes have displayed considerably enhanced specific capacitance value compared to the individual components, due to the synergetic effect between PANI and waste carbon particles. Thus, the present report will evidently encourage the waste management process with promising supercapacitor application as an added advantage.

Therefore, in this research work, we have demonstrated environment friendly cost-effective route to prepare waste carbon nanoparticles (WCPs)-incorporated PANI composite (Pa/WC) as electrochemical electrode material in supercapacitor applications. Pa/WC is synthesized via aqueous chemical polymerization technique by oxidizing aniline in presence of the carbon nanoparticles in direct step. Most importantly, the as-used carbon particles have been collected from normal cooking oven, thus, not only it relates the process to cost reduction issue, but also makes it sustainable and environmental benign. Different percentages of waste nanocarbon particles have been incorporated to determine their contribution towards the energy storage efficiency. Additionally, the effect of polymerization time on the electrochemical performance is also investigated in detail. All the materials are well-characterized by physical, spectral, electrical, electrochemical methods and are used as active electrodes in electrochemical cells. The supercapacitive properties of the Pa/WC electrodes are investigated by cyclic voltammetry (CV), galvanostatic charge-discharge (GCD) and electrochemical impedance spectroscopy (EIS) techniques. From all these studies, the combination of PANI and WCPs to form composites is demonstrated to be a very simple, cheap, and waste management recycling method to increase the specific capacitance of electrodes. The energy-storage of these supercapacitors combines two effects: A. pure electrostatic attraction of ions in the electrical double-layer from WCP and B. the contribution of pseudocapacitive Faradaic reactions from PANI backbone. Additionally, the WCPs within the PANI matrix, act as charge trapping layers via a distinct charge storage mechanism [26], due to which the specific

capacitance of the composite microelectrode is found to increase with increasing scan rate and current densities. This unique property indicates the suppression of diffusion limitations at higher scan rates/current densities to manifest excellent rate capability of the composite electrodes for superior supercapacitor applications. Besides, this process can be added as a new promising candidate of emerging green-energy technology era. Hence, the novelty of this work is the use of cooking oven-produced waste carbon nanoparticles as the carbon-source, to fabricate hybrid electrochemical microelectrodes for high-performance supercapacitors, which can be a great substitute for the costly and unsustainable source materials, thus stepping towards the green energy-technology.

2 Experimental Section

2.1 Materials

In the present research work, waste carbon product of normal cooking oven has been utilized as the source of WCP for preparation of WCP-PANI powder samples. The waste carbon material has been collected from a normal cooking oven having natural gas as the fuel. Different types of foods including both vegetables and non-vegetarian ingredients are mainly roasted in the oven, and the blackish burnt remains, deposited in the oven grill, are collected as the waste product. Precisely, these waste carbon blacks are deposited at the bottom of the grill over several weeks, after which these waste materials are collected. This means, each time the roasting is performed, the old wastes, already present at the bottom of the grill, are being heat-treated (~250 ^{O}C) repeatedly, while new wastes are being deposited onto the old wastes. Therefore, the entire waste-deposits are repeatedly being heat-treated in a near-cyclic manner over several weeks. Due to this prolonged high-temperature treatment, these blackish-burnt-remains are converted into pure carbon nanoparticles (according to XPS and EDS analyses, shown in Fig. 1 and Fig. S1), while all impurities are being oxidized out.

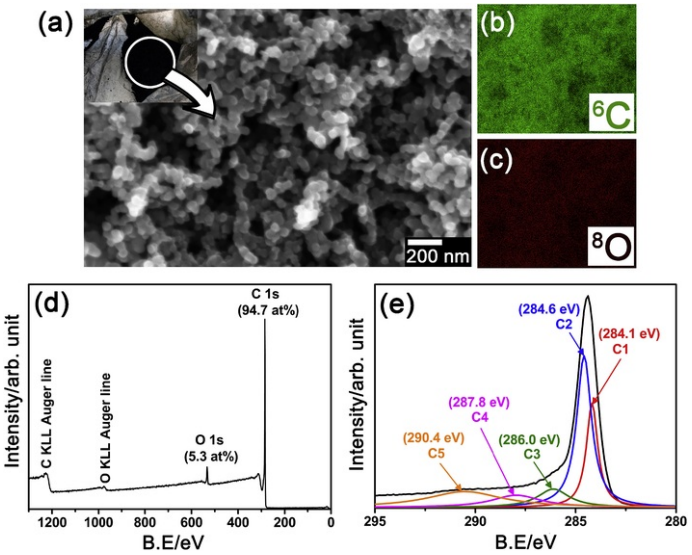

Fig. 1 (a) FESEM image of the as collected waste carbon nanoparticles (WCPs) which collected from standard household cooking oven. Left side top image shows the as collected WCPs. Before applying it in experimental design, we have gone through with EDS elemental mapping (and c) and XPS survey and C 1*s* high-resolution spectral analyses (d and e), respectively, of the WCPs. The study confirms the wastage carbon products collected from the oven are pure carbon material.

alt-text: Fig. 1

Moreover, we have collected these waste carbons not only from a single household kitchen oven, but also from the other household kitchen ovens, deposited in a similar fashion. All of them have shown the same chemical nature. This clearly indicates that, if the waste carbon formation process follows similar pattern as described above, then the waste product will be pure carbon particles, indicating that the process is highly reproducible.

To further corroborate the reproducibility of these waste carbon particle formation, we have performed the XPS analyses of the waste products collected from three different household kitchen ovens as mentioned above (Fig. 1d/e and Fig. S1). In all cases, the waste carbon formation process follows almost similar steps as described above. The XPS graphs and related elemental compositions again reveal that in all cases, the waste material is pure carbon, corroborating the fact that the prolonged high-temperature treatments converted the waste food products into pure carbon nanoparticles. Subsequently, these waste carbon nanoparticles are used in the composite material without performing any pre-treatment process.

In general, the food wastes mainly consist of carbohydrates, proteins, lipids, and traces of inorganic compounds, the compositions of which vary in accordance with the type of food waste and its constituents. Particularly, food waste consisting of vegetables is abundant in carbohydrates whereas food waste consisting of meat has high quantity of proteins and lipids [27]. In either case, since these ingredients are basically hydrocarbons, hence under roasting at high temperatures over a long period of time, these waste foods convert into carbon particles.

As the used material is purely carbon and we didn't need to do any further purification or chemical modification, therefore whole procedure is cheaper and environment friendly than the conventional ones. Most importantly, as both the oven and the roasted and burnt food wastes are commonly used in most of the everyday households, hence there is universality in the waste material. The novelty of this work is that, probably for the first time, the idea of using this food waste product in practical supercapacitive applications is pursued, and therefore, the microstructural and compositional analysis is performed for potential usability in electrochemical devices.

Aniline monomer (Sigma-Aldrich) is distilled under vacuum prior to use. All other reagents *e.g.* ammonium persulfate (APS; 99.99%, Sigma-Aldrich), hydrochloric acid (HCl; 35%, Alfa Aesar), camphor sulfonic acid (CSA; 99%, Sigma-Aldrich) and absolute ethanol (>99.99%, Alfa Aesar) are used as received without any further purification. Deionized (DI) water has been used during the experiments (obtained from Millipore Elix Advantage 3 purification system).

2.2 Preparation of Pa/WC (polyaniline-waste carbon composites)

The complete synthesis process is done in ethanol-water media (1:1 v/v). At first, the WCP is mixed in 10 mL ethanol-water solution by agitation with magnetic bead until it makes a stable dispersion. For different sample preparations, different amounts of WCPs are used (1, 2 and 4 wt% for Pa/WC*1*, Pa/WC*2* and Pa/WC*3* respectively). The WCP is incorporated into PANI as follows: During the typical chemical oxidative polymerization method in an ice bath, the aniline monomer was polymerized by using APS, HCl and CSA as oxidant, dopant and structure directing agent respectively. At first, aniline is dropwise mixed to 20 mL of ethanol-water solution and then, CSA is added (molar concentration of aniline: CSA = 1:0.25) to form the aniline-CSA complex. This mixture is then cooled at 0 °C for next 20 min. Afterwards, APS and HCl (molar ratio, APS: HCl: Aniline = 1:1:1) are added to the WCP dispersion (10 mL) which is already pre-cooled at 0 °C. Then this is drop by drop added to the monomer solution with vigorous shakings. The reaction is performed in a system maintained at 0 °C without stirring. For all the different concentrations of WCP, samples are also prepared with different polymerization time variations, for example, 1.5 h (t_1), 2 h (t_2), 2.5 h (t_3) and 3 h (t_4). Therefore, a total set of 12 composite samples were prepared with the nomenclature: Pa/WCx-t_y [x = 1 to 3 for three different wt% of waste carbon nanoparticles (1, 2, 4 wt %), and y = 1 to 4 for four different polymerization times (1.5, 2.0, 2.5, 3.0 h), respectively]. After the reaction is finished, the precipitate is collected through filtration. The greenish black product material is thoroughly washed with DI water for several times and then finally with methanol to get rid of the un-reacted monomer and oligomers. The product is ready for further tests only after it is dried in vacuum at 60 °C for the next 24 h.

2.3 Preparation of Pa/WC electrochemical electrodes

The electrochemical microelectrodes are fabricated by depositing the samples on glassy carbon electrode (GCE). Firstly, the GCE is polished with alumina powder (0.05 μm size) using CH Instrument (CHI) polishing kit, followed by rinsing with DI water and drying at room temperature (RT). Thereafter, slurry of samples is prepared by dispersing 5 mg of samples in 0.1 wt% nafion (NF)-contained 1 mL ethanol solution and sonicated for 10 min. Then, 5 μL of this dispersion is drop-casted onto the surface of GCE and dried at RT. Finally, the GCE is rinsed with DI water to remove loosely bound samples on the surface. The electrodes were having a planar structure with a working area around 0.07 cm^2. For comparison, similar electrodes are fabricated using pristine-waste carbon nanoparticles and pristine-PANI as active materials (named as WCP and PANI, respectively), which are considered as the control samples. Additionally, another electrode is fabricated using only nafion on the GCE (named GCE + NF). It has been confirmed (shown in Results and Discussion part) that the GCE + NF has negligible electrochemical properties, indicating that it has no contribution towards the electrochemical properties on the Pa/WC samples, *i.e.* all the electrochemical performances are purely being originated from the active materials.

2.4 Characterization

Differential scanning calorimetric measurements (DSC) of Pa/WC with different WCP concentrations were carried out using a Simultaneous Thermal Analyzer (TGA-DSC-STA 449 F3 Jupiter) from Netzsch. In an open Pt-Rh crucible around 5–7 mg of each sample was loaded, and then, heated starting from room temperature to 900 °C with a 10 °C min^{-1} heating rate in nitrogen atmosphere. Morphological and compositional analyses are done by a field emission scanning electron microscope (FESEM-FIB, Carl Zeiss Auriga Crossbeam microscope) with EDS (Oxford XMax 150). For X-ray photoelectron spectroscopy (XPS), a Kratos Axis Supra spectrometer was used with a monochromatic Al Kα source. The X-ray power was 225 W and a pass energy of 5 eV was used for the detail spectra. The fitting of the C 1s line with CasaXPS is similar to previous work [28]. The powder samples are further characterized by Raman (Renishaw Qontor InVia Raman microscope) spectroscopy using the 532 nm excitation laser line with 10% of the max. Laser power (50 mW) and 1s exposure time for each 10 accumulations. Atomic force microscopy (AFM) measurements are performed within an Asylum Research MFP-3D Stand-alone using commercial Pt-Ir tip coated probes. All the data were recorded under different applied bias, implying throughout calibration of the probe beforehand. The data are analyzed offline with the Asylum Research tools, developed within the IGOR Pro 6.22A data analysis software. The Brunauer–Emmett–Teller (BET) surface area of hybrids was determined by using N_2 adsorption/desorption measurements at 77K with an automatic surface analyzer (Micrometrics ASAP 2000 instrument, USA). Prior to the measurements, the samples were degassed in a vacuum at343 K for 24 h. The pore volume and

pore size distributions were estimated by using the Barrett–Joyner–Halenda (BJH) model.

2.5 Electrochemical characterization

The electrochemical measurements are conducted in an electrochemical work station, CHI 760 E using three electrode systems of GCE modified with samples as a working electrode, Pt-wire as a counter electrode and Ag/AgCl as a reference electrode. 1.0 M KCl solution is used as the electrolyte. The samples are subjected to:

(a) Cyclic Voltammetry (CV) measurements between −0.2–1 V at different scanning rates (10–100 mV s^{-1}). The areal capacitance (C in F cm^{-2}) from CV curves is calculated by integrating the area under the curves based on the following equation [29]:

$$C = \frac{1}{Av\left(V_2 - V_1\right)} \int_{V_1}^{V_2} I\ (V)\, dV \quad \textbf{(1)}$$

where ν (V s^{-1}) is the scan rate, (V_2-V_1) is the potential window (V), I is the current (A) and A (cm^2) is the area of the working electrode (0.07 cm^2).

(b) Galvanometric charge-discharge (GCD) methods by varying current densities (15–100 μA cm^{-2}). The areal capacitance from GCD curves is calculated according to the following equation [29]:

$$C = \frac{I\ (\Delta t)}{(\Delta V) A} \quad \textbf{(2)}$$

where I is the discharge current(A), Δt is the discharge time(s), ΔV is the attainable cell voltage (V) *i.e.* the potential change during discharge after IR drop (V_{max} – V_{IR}) and A (cm^2) is the active area of the electrode.

(c) Electrochemical impedance spectroscopic (EIS) measurements are performed at an open-circuit potential (OCP) between 0.1 Hz and 100 kHz with an AC perturbation of 5 mV. The EIS data are fitted with an equivalent circuit to determine various electrochemical parameters like series resistance (R_Ω), charge-transfer resistance (R_{ct}), constant phase element (CPE_{DL}) and Warburg coefficient (Ψ_w). Also, the energy-power performance of the composite electrode is measured from the following equations (using GCD data) [30]:

$$\xi = \frac{C\ (\Delta V)^2}{2\ \times 3600} \quad \textbf{(3)}$$

$$\Phi = \frac{E \times 3600}{\Delta t} \quad \textbf{(4)}$$

where ξ (in Wh cm^{-2}) is the areal energy density, Φ (in W cm^{-2}) is the power density, ΔV (in V) is the potential drop after a full discharge, C is the areal capacitance (in F cm^{-2}) and Δt is the discharge time (in sec).

3 Results and Discussion

3.1 Materials properties

3.1.1 Thermal behavior and chemical composition and surface analyses

The waste carbon particles (WCP) has been examined by FESEM with EDS elemental mapping, and the morphology and composition analyses have proved it to be made of pure carbon nanoparticles as shown in Fig. 1(a)-(c). We have further examined the surface states and elemental composition of the samples via XPS tools. Fig. 1(d)/(e) shows the XPS survey and C 1*s* high-resolution spectra, respectively, of waste carbon product collected from a standard household cooking oven. The elemental composition is given in the survey spectra. The study again confirms that the wastage carbon products collected from the oven are pure carbon material. The high-resolution C 1s spectrum is deconvoluted into 5 components. Peak C1 corresponds to sp^2 hybridized carbon (graphitic carbon), peak C2 is for sp^3 hybridized carbon, peaks C3 is due to the C in C-O bonds, peak C4 is the carbonyl C (C=O) and peak C5 corresponds to the carboxylate C (O-C=O) [19,31]. The O 1s peak originates from the carbonyl and carboxyl groups and also from some probable surface-bound atmospheric hydroxyl groups (attached during sample preparation and handling). To further verify the reproducibility of the waste carbon particle formation process, the waste materials were collected from two other household kitchen ovens and presented in Fig. S1. In all cases, the waste carbon formation process follows almost similar steps as described in the Experimental section. Both the survey and high-resolution C 1s spectra are found to be similar to that of Fig. 1(d)/(e), indicating that the waste materials are pure carbon nanoparticles, and no impurities are present (within the instrumental limit). Since XPS is a highly reliable characterization process with high-sensitivity, and used routinely (both in laboratory scale as well as in industrial scale [32] to evaluate the elemental composition of various materials, therefore, absence of any elemental component in the XPS data can authentically be considered to be either completely absent or too low to affect the physicochemical and/or electrochemical properties of the materials.

The composites of polyaniline-waste carbon nanoparticles (Pa/WC) are synthesized through in-situ polymerization of PANI, without any further chemical modification or purification of waste carbon product. The whole procedure is therefore cheaper and environment friendly than the conventional ones. Three types of composites with different concentrations of WCPs have been synthesized. Each amount of carbon nanoparticles, functionalized into polyaniline has been synthesized for four different polymerization stages associating with different reaction times (t_1: 1.5 h, t_2: 2 h, t_3: 2.5 h, t_4: 3 h). All the specifications of samples have been elaborately mentioned in the "Experimental Section". A typical FESEM image of Pa/WC*3*-t_4 composite is shown in Fig. S2a (Supporting Information). The figure consists of porous near-spherical PANI aggregate containing carbon nanoparticles inside it. It must be mentioned in this connection that we have not individually coated each carbon nanoparticles with 400–500 nm layer of PANI to make it a core-shell structure. Instead it has been clearly described that the carbon nanoparticles are dispersed in the oxidizer based precursor, which is then mixed to the aniline-CSA complex-based precursor to get polymerized and after a certain polymerization time it forms into porous near-spherical aggregates, containing several carbon nanoparticles within each sphere of 400–500 nm thick PANI layer, as described in the schematic diagram (Fig. S2b, Supporting Information) and confirmed by the Electrostatic Force Microscopic (EFM) analysis (Fig. 2). Especially, the EFM mapping for Pa/WC*3*-t_4 composite (Fig. 2a) is showing the presence of 4 carbon nanoparticles (WCPs) embedded in a 500-nm polyaniline near-spherical structure, thus confirming our claim. Generally, EFM is used under the applied positive bias to characterize the local charge density in the PANI matrix [33,34]. Charged areas are observed as dark spots with negative phase shift, which is the indication of localized charge trapping at the midpoints, created by WCPs. The corresponding line profile (in Fig. 2b) shows that the FWHM of the charge midpoint is around 80 nm. This is quite well matched with the size of embedded WCPs which is around 40–50 nm (shown in FESEM figure). Also, thermodynamically, there will be a statistical variation of nanoparticle position with respect to the PANI surface, which means, some WCPs can be situated close to PANI surface (shallow position) and some deep inside the PANI film (interior position). Additionally, due to the porous structure, there will be high probability of some of these shallow nanoparticles to be exposed to the active electrolyte through the pores during electrochemical measurements and contribute to the overall supercapacitive performance of WCP-PANI composite (discussed in detail later).

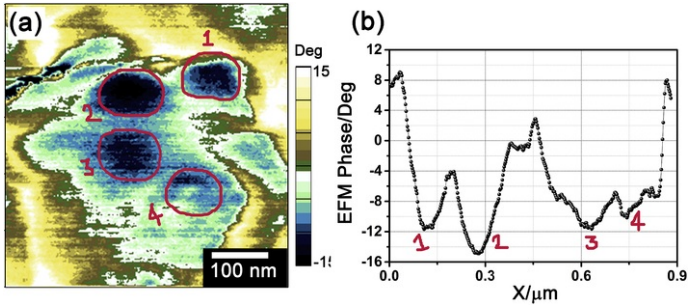

Fig. 2 (a) EFM mapping showing the local charging effect of WCPs embedded in Polyaniline matrix deposited on ITO coated glass substrate. (b) Corresponding line profile of four charge mid-points indicates carbon nanoparticles (with FWHM 80 nm, which are well-matched with the WCPs sizes found in FESEM). An offset is applied to all colour scales so that they are centered on the average value of the surface potential over the PANI matrix.

alt-text: Fig. 2

Detailed information about the thermal behavior of as-synthesized WCP-PANI composites has been investigated by thermogravimetry analysis (TGA) and differential scanning calorimetry (DSC) analysis. Fig. 3a-c shows the major weight loss stages for the samples with different concentrations of WCPs (Pa/WC*1*-t_4, Pa/WC*2*-t_4, Pa/WC*3*-t_4 prepared with t_4 reaction duration) to see the effect of incorporating WCPs in the polymeric backbone. The first stage of weight loss (~6–7%), which has occurred in the range 30–150 °C, is attributed to the loss of moisture, some oligomers with low molecular weight and residual solvents [35]. The second stage of weight loss (~6–10%) has started around 180 to 300 °C which can be due to the decomposition of non-bounded sulfonic acid dopant. The third major stage, starting after 500 °C, is corresponding to the degradation of the skeletal PANI chain structure [36]. This degradation temperature for PANI chain is slightly higher than pristine PANI as reported elsewhere [37], which can be correlated to the incorporation of WCPs that increases the thermal stability of the polymer backbone. Also, it is noticed from Fig. 3 that the thermal degradation of the Pa/WC samples shifts towards higher temperatures as the concentration of WCPs is increased. This signifies the interactions between macromolecular PANI chains and WCPs, revealing the formation of polyaniline-carbon interface with enhanced thermal stability.

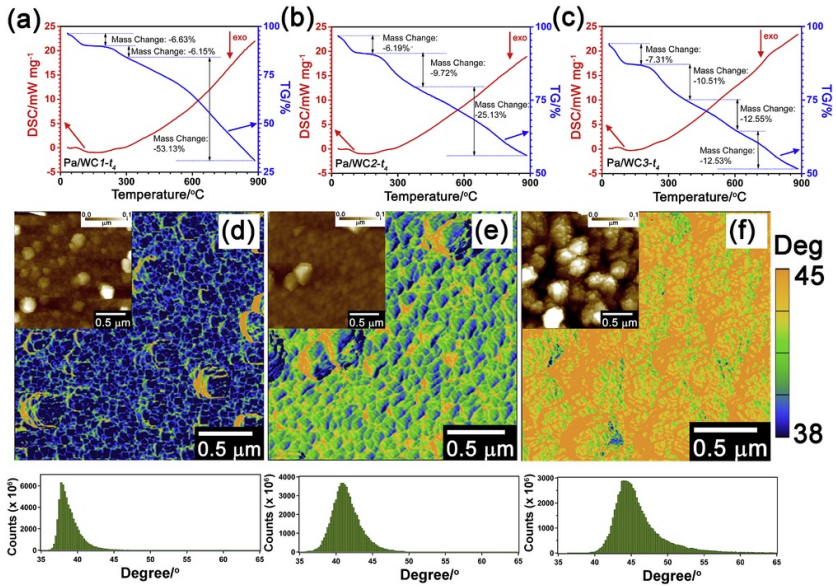

Fig. 3 Study of TG-DSC and PI-AFM for (a)/(d) Pa/WC*1*-t_4, (b)/(e) Pa/WC*2*-t_4, (c)/(f) Pa/WC*3*-t_4, respectively. Inset of each figure (d), (e) and (f) shows the topography image of the corresponding samples. The histogram of each PI-AFM has been shown below, indicating different phase distribution according to percolation of WCP concentration into PANI.

alt-text: Fig. 3

Furthermore, to evaluate the impact of functionalization in the polyaniline-carbon composites, phase-imaging (PI) mode along with surface topography by atomic force microscopy (AFM) is used. The PI-AFM is a powerful tool for surface characterization of the soft composites materials (*i.e.* polymers or biomaterials), and the obtained phase image can detect chemical variation as well as is able to reveal more detailed surface properties than the morphological image [38–40]. Phase information is collected through the detection of phase shift between driving and actual tip response oscillation signals. From Fig. 3d-f, it can be observed that the average phase of the image is increased from 39° to 45° as the percolation of WCPs increases from sample Pa/WC*1*-t_4 to Pa/WC*3*-t_4. The phase shifts are due to different interactions of the AFM tip with the surface because of different chemical variations in the samples. The corresponding histogram of phase image has been shown below of each figure, the area of which is proportional to the percolation concentration of WCP within PANI. The evaluation of the histogram shows the broadening of the graph, indicating the increment in the amount of WCPs incorporated into polyaniline. Therefore, the ratio of the areas under the histograms for three samples will provide a qualitative information of the WCP concentration within PANI matrix. A quantitative calculation of the histogram areas for Pa/WC*1*-t_4, Pa/WC*2*-t_4 and Pa/WC*3*-t_4 indeed depicts a ratio of 1.00 : 2.05: 3.96, which is near-identical to the weight ratio of WCP within precursor solution (1 : 2: 4). This indicates that the carbon nanoparticles are uniformly dispersed into the precursor solution and efficiently replicates into the PANI-WCP composites. Also, similar trend is observed for all composites with different polymerization stages (*e.g.* Pa/WC*1*-*3*-t_1-t_3).

For a typical sample of Pa/WC*3* (with the highest concentration of WCPs), Raman spectra has been investigated for four different polymerization times. Fig. 4 reveals the influence of the interactions between WCPs and PANI components on the molecular structure of PANI phase with the different polymerization conditions. The figure represents typical Raman spectra acquired for Pa/WC*3* samples and WCPs, showing different evolutionary peak positions according to the polymerization time. All the characteristics Raman bands from PANI *i.e.* 1633, 1595 and 1561 cm^{-1} for Quinoid or Benzenoid rings C=C stretching modes, 1401 cm^{-1} for different C–N stretching modes (amines, imines, polarons, bipolarons), 1248 and 1170 cm^{-1} for C–H bending of the benzene rings have been observed [41–44]. As expected, all the peak intensities are observed to be increased with increasing polymerization time, apparently due to the strengthening of the polymer backbone. In addition to the PANI bands, “G” (1570 cm^{-1}) and “D” (1343 cm^{-1}) Raman vibrational bands from carbon particles have also been observed (the dotted lines) [43–45]. However, the peaks corresponding to G and D lines has been shifted to the lower wavenumber for the composites indicating well functionalization of WCPs into polymer matrix. Hence, all these facts indicate that the waste carbon nanoparticles are well-connected to the PANI backbone structure, with gradually better functionalization for increasing polymerization time.

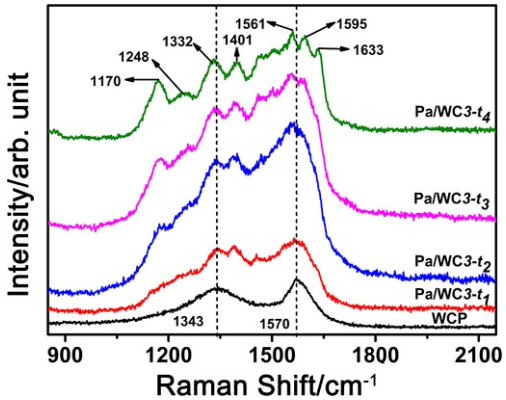

Fig. 4 Raman spectra of a typical sample series of Pa/WC*3*for different polymerization times. The spectrum in black shows the Raman of as-collected carbon particles (WCPs) from household waste product. Evolutions of Raman spectra with polymerization time (*i.e.* from t_1 to t_4) have been clearly distinguished.

alt-text: Fig. 4

3.1.2 Kelvin probe force microscopy

Moreover, Kelvin probe force microscope (KPFM) technique has been used to investigate the effects of polymer structure and interaction on percolation concentration of WCPs into the polymer matrix. The results obtained from studying a series of polyaniline-carbon composites with different polymerization times and different WCP concentrations has been illustrated in Fig. 5. KPFM measures the height variations on sample surface, and simultaneously employs the electrostatic forces through AFM tip, that allows to minimize the electrostatic interaction between tip-sample surface, which finally yields the surface potential difference (SPD) [46–48]. This type of technique can directly interpret the SP difference by measuring the localized work function of the sample surface ($\phi = _{sample}$) against the known cantilever work function (ϕ_{tip}), according to the relation: SPD = (ϕ_{sample}- ϕ_{tip})/e [48]. In Fig. 5 (right), SP difference mapping of all the 12 samples has been illustrated under sample colour scale ranging from −0.5–1.5 V. For each percolation concentration of WCPs into PANI, the surface potential gradually increases from lower reaction time to higher reaction time *i.e.* from t_1 to t_4. For Pa/WC*1* series, the surface potential increases from −0.32 to 0.05 V; for Pa/WC*2* series, SPD increases from 0.58 to 0.68 V and for Pa/WC*3* series, SPD increases from 0.57 to 1.2 V (from t_1 to t_4). And for highest polymerization time (*i.e.* t_4: 3 h), the SPD values change as 0.05 V, 0.68 V and 1.2 V for Pa/WC*1*, Pa/WC*2* and Pa/WC*3*, respectively. These KPFM studies of the surface potential topography for all the samples reveal two phenomena: (1) for a particular polymerization time, the average value of SPD is increased with the increasing amount of carbon particles into the polyaniline, and (2) for a particular WCP concentration, the average value of SPD is increased with the increment in the polymerization time. The former phenomenon indicates that, with the increase in WCP percolation concentration the work function of polyaniline is increased, which in turn supports the fact that the WCPs have acted as charge trapping-layer within the polyaniline system [26]. Whereas, the later phenomenon is ascribed to a weak interaction between WCPs and PANI in the preliminary stage of reaction at lower polymerization time, and with the increase in time (from $t_1$to t_4), WCPs (incorporated within PANI) lead to a strong π-π interaction.

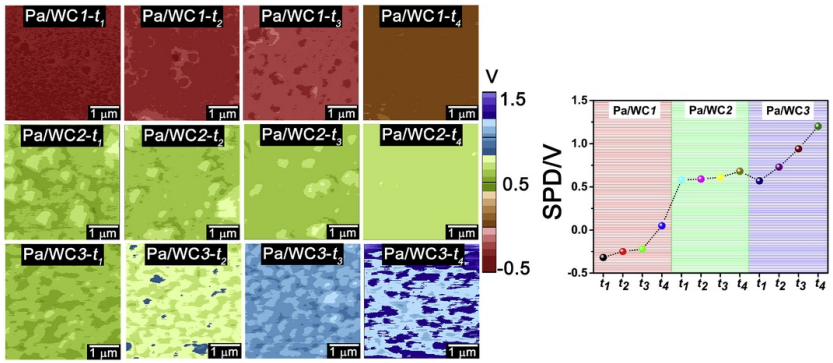

Fig. 5 An evolutionary KPFM image of WCPs-PANI composites with different percolation amount of WCPs into PANI along with the polymerization time *i.e.* the reaction time of WCPs with PANI through the in-situ polymerization of polyaniline. Gradual increment of surface potential has been noticed with WCPs concentration into PANI as well as increasing polymerization time. A comparative profile of average surface potential calculated from the KPFM scanning image ($4 \times 4\ \mu m^2$) with both polymerization time and WCP concentrations has been shown (right

image).

alt-text: Fig. 5

The BET N_2 adsorption/desorption isotherms of all the samples are presented in Fig. 6. The isotherms have characteristics of a type IV with type H3 hysteresis loop, indicating mesoporous nature of the surface [49]. The BJH pore size/volume distribution is presented in the inset. All the BET-BJH parameters are shown in Table 1. The BET surface area (S_{BET}) and BJH pore volume (obtained from desorption curves) are found to increase with polymerization time, and for a particular polymerization time, the S_{BET} value increases with WCP concentration. Also, majority of the pore size distribution (shown in the insets) are found to be bimodal in nature, with a narrow pore size distribution around 3–4 nm and a wide distribution around 20–30 nm. The smaller (and narrower) ones are the near-uniform mesopores present on the surface of each PANI spheres, whereas larger (and wider) ones are manifested due to the agglomerated structure of the WCP-PANI spheres that create some pore-like microstructure in-between the spheres (as shown in FESEM micrograph in Fig. S2a, Supporting Information).

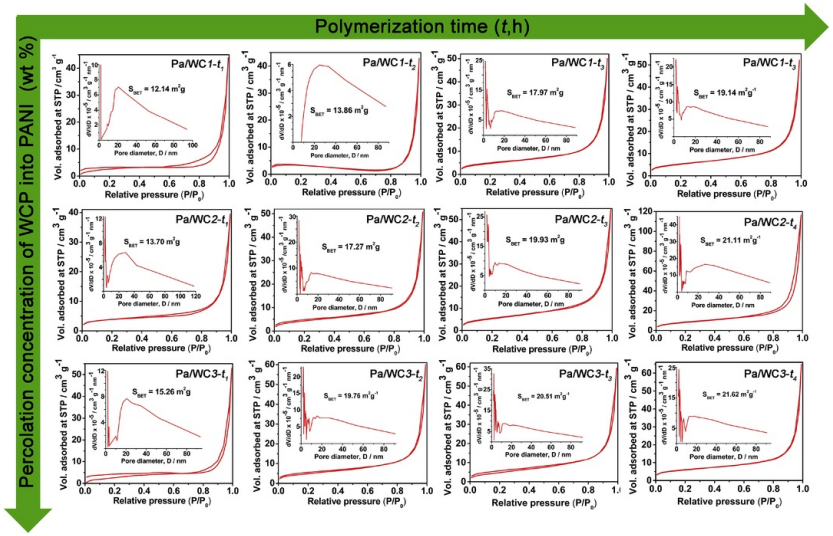

Fig. 6 BET N_2 adsorption/desorption isotherm curves for WCP-PANI composites. Insets: BJH pore size distribution.

alt-text: Fig. 6

Table 1 BET-BJH and roughness data of WCP-PANI composites.

alt-text: Table 1

Samples	BET surface area/m^2 g^{-1}	Avg. BJH pore volume/cm^3 g^{-1}	*rms* surface roughness/nm
Pa/WC*3*-t_1	15.26	0.081	35.1
Pa/WC*3*-t_2	19.76	0.090	40.7
Pa/WC*3*-t_3	20.51	0.091	58.7
Pa/WC*3*-t_4	21.62	0.097	71.3
Pa/WC*2*-t_1	13.70	0.068	25.6
Pa/WC*2*-t_2	17.27	0.075	29.9
Pa/WC*2*-t_3	19.93	0.083	34.6
Pa/WC*2*-t_4	21.11	0.090	37.6
Pa/WC*1*-t_1	12.14	0.065	14.9

Pa/WC*1*-t_2	13.86	0.066	17.5
Pa/WC*1*-t_3	17.97	0.076	25.7
Pa/WC*1*-t_4	19.14	0.078	29.8

In addition to the BET-BJH data, the surface roughness values of the electrodes are also measured via AFM topographic image analyses and are presented in Fig. S3 (Supporting Information) and Table 1. In addition to BET surface area, the root mean square (*rms*) roughness (*R*) value is also important, especially for interfacial applications (like electrochemical supercapacitor, as in the current case) of thin film devices/electrodes, which qualitatively provides the information about the active surface sites for higher utilization of active materials for superior electrochemical performance. All the roughness data are found within the sub-micron range, indicating relatively high active surface sites of the thin film electrodes for better supercapacitive performance. In accordance with the BET data, the roughness value is also found to increase with polymerization time. Also, for a particular polymerization time, the *rms* roughness increases with WCP concentration. The apparent reason is that, with initialization of polymerization process, the micellar aniline-CSA complex starts to incorporate the WCPs within its polymeric skeleton and begins to form the primary nano-assemblies of WCP-PANI. With increasing time of polymerization, while including more WCPs within the backbone, the polymeric part in presence of dopant CSA (as structure directing agent) grows more towards an aggregated composite material structure following directional secondary growth from the existing polymer seeds; Henceforth, the roughness is found increasing with increasing polymerization time as well as with increasing WCP concentration.

3.2 Electrochemical analyses

3.2.1 Cyclic voltammetry

The Cyclic Voltammetry (CV) curves in Fig. 7 for control samples (WCP, PANI) at different scan rates show typical double layer capacitance of waste carbon nanoparticles with quasi-rectangular shape (WCP, Fig. 7a) and pseudocapacitive behavior of polyaniline with two pairs of redox waves (O^1-R^1/O^2-R^2) (PANI, Fig. 7b). These Faradic oxidation-reduction peaks have originated from the electron transfer from electrolyte-to-PANI (O^1) and PANI-to-electrolyte (R^1) (leucoemeraldine-to-emeraldine transition of PANI), and deprotonation (O^2)/protonation (R^2) (emeraldine-to-pernigraniline conversion). The widenning of the redox peaks is a result of overlapping of the two redox processes in aqueous medium, which is a commonly observed phenomenon [18,50,51].

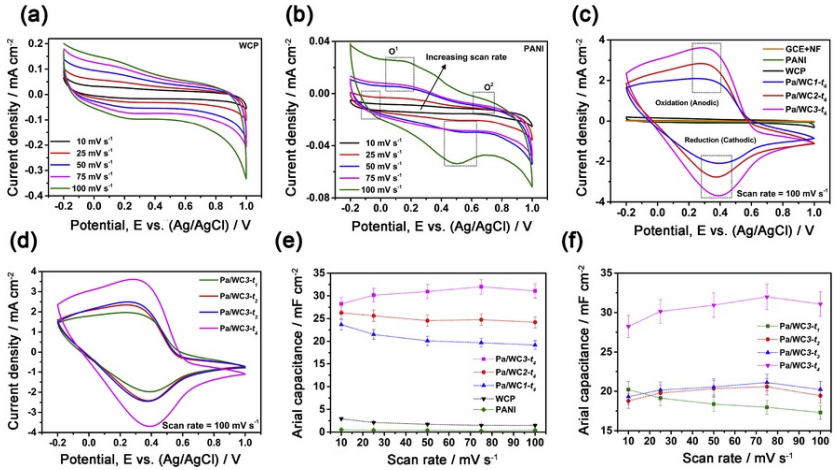

Fig. 7 CV curves at different scan rates for (a) waste carbon nanoparticles and (b) PANI. (c) Comparison of the CV curves for three different composite samples at constant polymerization time t_4 = 3.0 h with control samples and GCE + NF electrode, (d) comparison of the CV curves for Pa/WC*3* composite at four different polymerization times (t_1-t_4), (e) comparison of the areal capacitance as a function of scan rate for three different composite samples at constant polymerization time t_4 = 3.0 h with control samples, (f) comparison of the areal capacitance as a function of scan rate for Pa/WC*3* composite at four different polymerization times (t_1-t_4).

alt-text: Fig. 7

To observe the electrochemical performance of the hybrid electrodes, CV curves of the composite samples (Pa/WC) at three different WCP concentrations (1.0, 2.0 and 4.0 wt% for Pa/WC*1* to *3*, respectively) at a constant polymerization time (t_4 = 3 h) is presented in Fig. 7c, alongwith the control samples (WCP and PANI) and the GCE + NF electrode. Evidently, GCE + NF electrode shows negligible electrochemical properties, indicating that the electrochemical properties of all the prepared

samples are entirely originating from the active materials. The CV curves for the composite samples depict the typical combination of electrical double layer capacitance (EDLC) of WCPs and pseudocapacitance of PANI. The larger quasi-rectangular areas and higher anodic and cathodic currents of the composite electrodes (an increment of almostone-to-two orders of magnitude) against the control samples indicate signficant EDLC effect because of the presence of WCPs within the composite in high concentration, which act as electron trapping centers during the electron transfer from electrolyte to the PANI (Oxidation), resulting in higher electron-transfer-rate, thus enhancing the anodic current. This is also the reason for the suppression of one of the redox pairs (O^2-R^2) in the composite samples. Additionally, the CV curves (at different scan rates) of all the samples at three different WCP concentrations (Pa/WC*1* to *3*) and four different polymerization times (t_1 to t_4) are compared in a two-dimensional array at Fig. S4 (Supporting Information). Most of the samples depict the typical combinatorial effect of double-layer capacitance (of WCP) and pseudocapacitance (of PANI). For Pa/WC*1*-t_1 sample, this combinatorial effect is less pronounced, mainly because, in this case the CV area and the current have shown very small values. Although for Pa/WC*1*-t_2 sample, the current is increased one order of magnitude against Pa/WC*1*-t_1, but still it is considerably lesser than that of other samples. The reason is mainly due to lesser WCP concentration and polymerization time in these samples for charge trapping to be effective. This indicates that both the WCP concentration and polymerization time have significant effect on the hybrid electrochemical properties of the composite electrodes, and there are some optimum values of WCP concentration and polymerization time, below which the combinatorial effect of EDLC and pseudocapacitance is not effective in the hybrid electrode.

Therefore, to get a perspective of the effect of WCP concentrations on the supercapacitive performance of composite electrodes, the CV curves (at 100 mV s^{-1} scanrate) of the composite samples at three different WCP concentrations (and at a constant polymerization time, *t*) is presented in Fig. S5a-d, Supporting Information. In all cases, for a particular polymerization time, the Pa/WC*3* (4 wt% of WCP) depicts the best CV performance against other samples (Pa/WC*1*/*2* with 1/2 wt% of WCP, respectively). This is mainly due to the increment of work function of polyaniline as an increasing function of the WCP percolation concentration (as obtained from KPFM technique, shown in Fig. 5), leading to higher trapping of charges at higher WCP concentrations. Therefore, with the increase in the waste carbon concentrations within PANI matrix, the charge storage capabilities of Pa/WC composites have been alsoenhanced. As far as the effect of polymerization time on the electrochemical properties of the hybrid electrode is concerned, Fig. 7d and S5e-f (Supporting Information) represent the polymerization time variations (t_1 to t_4) of CV curves for the same WCP concentrations. In all cases, CV performance increases with increasing polymerization times and the largest polymerization time ($t_4 = 3$ h) produces highest CV performance. This is apparently due to the better interfacial properties between waste carbon nanoparticles and PANI at higher polymerization time that leads to the better charge trapping and transport properties of the composites for superior electrochemical performance.

The areal capacitances of all the samples (as a function of scan rates) are calculated from Eqn. (1) and have been presented in Fig. 7e-f and S6a-f (Supporting Information), respectively. For example, Fig. 7e compares the scan rate variations of the areal capacitances of composites at three different WCP concentrations (for a constant polymerization time, t_4) with the control samples (WCP and PANI). Evidently, composite electrodes reveal considerably higher C-values against the control samples, which is consistent with the CV data discussed above. Similarly, comparisons of the scan rate variations of C-values of composite electrodes at three different WCP concentrations (Pa/WC*1* to *3*) for a certain polymerization time (*t*) (*cf.* Fig. S6a-d, Supporting Information) depict highest C-values for Pa/WC*3* sample (having highest WCP concentration of 4 wt%), which is in agreement with the CV data. As far as the effects of polymerization time on C-values of the composite samples are concerned, highest polymerization time ($t_4 = 3$ h) shows best C-values for a certain WCP concentration (*cf.* Fig. 7f and S6e-f, Supporting Information) which is again consistent with the CV results. The C-values, calculated from CV data for all the samples, are presented in Table S1 (Supporting Information), which depicts the best supercapacitive performance for Pa/WC*3*-t_4 sample with the highest areal capacitance around 32 mF cm^{-2} at a scan rate of 75 mV s^{-1} (highlighted in red). Therefore, for the current samples, theoptimum 4 wt% carbon nanoparticle concentration within PANI matrix with an optimum polymerization time of 3 h produces the best supercapacitive performance of the Pa/WC hybrid electrodes.

It must be mentioned here that we have calculated areal capacitance (mF/cm^2) of the electrodes instead of gravimetric capacitance (F/gm) due to the fact that for nanoporous carbon materials (deposited on glassy carbon substrate, as in the current case) the EDLC depends mainly on the active surface area, which correlates to higher utilization of the active materials. Higher is the porosity and roughness of the electrode surface, higher are the active surface sites, greater is the utilization of the active materials, and hence, larger is the capacitance value. Therefore, areal capacitance is scientifically more relevant [52]. To verify this, firstly we have calculated the mass of the active material via differential weight measurement (weight difference between coated and uncoated glassy carbon surface with active material), which gives a value around 25–30 μg. Thereafter, using this value, the gravimetric capacitance for Pa/WC*3*-t_4 sample (best performing electrode) at 75 mV s^{-1} scan rate is calculated using the following equation [53]: $= \frac{1}{2m\nu\,(V_2 - V_1)} \int_{V_1}^{V_2} I\,(V)\,dV$; where ν (V/s) is the scan rate, (V_2-V_1) is the potential window (V), I is the current (A) and m is the mass of the active material (g). The gravimetric capacitance is obtained around 90 F/g, which is higher than the areal capacitance for the same sample at the same scan rate (31.99 mF cm^{-2} @75 mV s^{-1}, *cf.* Table S1). But if we compare this value with the literature report of similar PANI-carbon nanomaterial electrodes, where gravimetric capacitance is calculated from CV data [20,54], then we will see that the active mass used in those reports are in the milligram range (which is three orders of magnitude higher than the current report), whereas the gravimetric capacitance (~300–400 F/g) is only one order of magnitude higher than the current report. This indicates exceptionally high gravimetric capacitance in our samples relative to the mass loading, which reiterates the fact that considerably high utilization of the active material is manifested in our electrodes due to the nanoporous surface with high active surface sites. Hence, we believed that areal capacitance is scientifically more realistic parameter to properly represent the capacitive performance of our electrode. That is why we have used areal capacitance throughout the manuscript.

Additionally, from all the areal capacitance versus scan rate plots for composite electrodes (*cf.* Fig. 7e-f and Fig. S6a-f in Supporting Information), it has become evidenced that with an increase in the scan rates, in majority of cases, the C-values remain near-constant (within 5%, as shown by the error bars). In fact, instead of deterioration, the areal capacitance increases in some cases with the increase in the scan rate. For example, Pa/WC*3*-$t_{1\text{-}4}$ composites and some of the Pa/WC*2* composites reveal an increment of the C-value with the increase in the scan rate up to 75 mVs^{-1}, and then decrease slightly at 100 mVs^{-1} (*cf.* Figs. 7f and S6-Supporting Information). This is eventually due to the unique charge trapping mechanism of the carbon nanoparticles within PANI (explained below), which indicates excellent rate capability of the composite electrodes [55].

It must be mentioned in this connection that, generally in most of the cases, due to the diffusion limitation, the specific capacitance decreases with increase in the scan rate [56–58]. This would be more pronounced for quasi-reversible/irreversible electrochemical processes due to the 'slower' charge-transport/-distribution kinetics against the voltage scan rate (*cf.* Fig. S7). There are very few reports (to best of the authors' knowledge) that have shown an increase in the specific capacitance value with increase in the scan rate. For example, Lang and co-authors [57] have observed an increment in the specific capacitance value of gold/MnO_2 electrode with the increase in scan rate from 10 mVs^{-1} to 50 mVs^{-1}, which is attributed to higher active surface sites into the porous structure alongwith higher conductivity of the gold plating that enhances the charge transfer capabilities. In the current case, the increment in C-values with the scan rate is due to the dual effects of high active surface sites of nanoporous PANI-carbon nanoparticle structure (as explained in Fig. S8), and the unique charge trapping mechanism of the waste carbon nanoparticles (as schematically shown in Fig. 8), that increases the current density across the interface of the electroactive material and the electrolyte (for EDLC process) [58,59]. Especially for the latter case (charge trapping phenomenon), although the current electrochemical system follows a surface-controlled quasi-reversible process [60–62] (*cf.* Fig. S7), but the faster change in the surface potential at higher scan rates generates a high local electric field at the electrode-electrolyte interface as well as across the electroactive material [58,59]. Due to this, the barrier height across the carbon nanoparticle (assuming columbic barrier potential) is reduced along the direction of the applied field. This has made the charge trapping at the waste carbon nanoparticles more effective (the process is explained in the caption of Fig. 8). Consequently, the current density becomes higher due to higher flux of ions towards the electrode-electrolyte interface (to maintain charge neutrality in the EDLC process), which masks the diffusion limitation and increases the area under CV curves to enhance the C-values at higher scan rates [58]. Due to the same reason, the areal capacitance of the composites, obtained from GCD studies (shown in Fig. 8f), is observed to be either increased or remained near-constant with the increase in current density, indicating that the distinct charge trapping process of carbon nanoparticles within PANI increases the discharging time considerably to enhance the C-values at higher current densities.

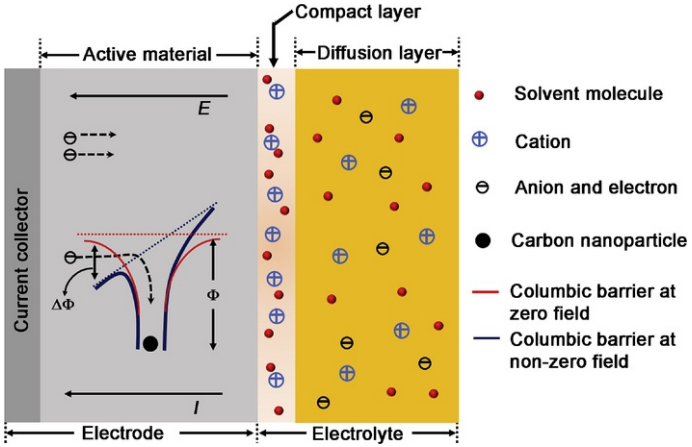

Fig. 8 Schematic representation of charge trapping mechanism within PANI-carbon nanoparticle system. Assuming Columbic potential barrier across the carbon nanoparticles (red lines, at zero field), during anodic sweep, under the applied field, the barrier height (φ) will be reduce by a factor $\Delta\varphi$ in the direction of the applied field (blue lines), which would make the charge trapping energetically more favorable. At the higher scan rates, the increment in the local electric field manifests higher reduction of the barrier height in the direction of the applied field, which, in turn, makes charge trapping more effective. Similarly, during cathodic sweep, reverse phenomenon would occur (*i.e.* more release of trapped charges at higher scan rates). (The diagram is not to scale). (For interpretation of the references to colour in this figure legend, the reader is referred to the Web version of this article.)

alt-text: Fig. 8

Obviously, there must be a thermodynamic limit of the scan rate for the above-mentioned two mutually competing processes to dominate one over the other. For too higher voltage sweeping rate (*i.e.* at very high scan rate), diffusion would become the limiting factor again. Evidently, in the present case (for Pa/WC*3*-t_2-to-t_4 and some of the Pa/WC*2* composites), the above phenomenon dominates up to 75 mVs^{-1} scan rate (*i.e.* C-value increases with scan rate), and beyond that, the diffusion limitation starts dominating (*i.e.* C-value decreases slightly at 100 mVs^{-1} scan rate), mainly due to considerably quicker voltage sweeping rate as discussed above.

We have also estimated the electrochemical surface area of the electrodes (A_{EC}, in cm^2) using Randles-Sevcik equation for quasi-reversible process (as in the current case described in Fig. S7). The calculated values of A_{EC} at different scan rates are presented in Fig. S9 for Pa/WC*3*-t_4 sample (best performing electrode, as shown in Tables S1 and S2), which range from 0.01 to 0.03 cm^2 at different scan rates. For other samples also this value varies approximately within this range. But these values appear to be considerably smaller than expected (especially for porous materials used in the current case where the working area is 0.07 cm^2), which indicates that the calculated A_{EC} values are not quite reliable. The apparent reason is that the Randles-Sevcik equation is mainly applicable to relatively flat and non-porous electrode surface, where, over the timescale of the voltammetric experiment, the diffusion layer should be larger than the surface micro-features of the electrode to manifest heterogeneous electrode kinetics [63]. But in the current case, the samples are highly porous, with high surface roughness, as depicted by the FESEM micrographs and AFM topographic images (Figs. S2 and S3), which indicates that the electrode surface micro-features are comparable and/or lesser than the diffusion length, and hence go undetected, leading to underestimated values of electrochemical surface area.

3.2.2 Galvanostatic charge-discharge curves

Galvanostatic charge-discharge (GCD) curves for control samples as well as composite electrodes at various current densities are presented in Figs. 9 and S10 (Supporting Information). Fig. 9a presents the GCD curves for WCP electrode. The almost triangular shape of the curves with near-linear charging curve indicates typical double layer capacitance of carbon nanoparticles [50,64]. Fig. 9b represents the GCD plot for pure PANI electrode, which depicts considerable deviation from linearity of the curves, indicating pseudocapacitive behavior of PANI [65]. Fig. 9c compares the GCD curves of the composite electrodes (for three different WCP concentrations *i.e.* 1, 2 and 4 wt%, and at a constant polymerization time t_4 = 3 h) with the control samples (WCP and PANI) and the GCE + NF electrode. The GCE + NF electrode shows negligible capacitive behavior, thus reiterating the CV results that it has no contribution to the capacitive properties of the active materials. The charge-discharge curves for composite electrodes are extended considerably against the control electrodes, indicating excellent electrochemical properties of the composite samples due to the combinatorial effect of EDLC (from WCP) and pseudocapacitance (from PANI). Among the three composite electrodes (Pa/WC*1* to *3*at t_4), some interesting facts emerged from Fig. 9c: (*i*) For the samples with lower WCP concentrations (Pa/WC*1*-t_4, 1 wt% and Pa/WC*2*-t_4, 2 wt% of WCP), the charging curves deviate slightly from the linearity, indicating the combinatorial effect (pseudocapacitance + EDLC) is less effective, whereas this part deviates considerably in the Pa/WC*3*-t_4 (4 wt % of WCP) sample, indicating that the combinatorial effectis highly effective. (*ii*) In the discharge curves, for Pa/WC*1*-t_4 and Pa/WC*2*-t_4 composites, after a shorter IR drop (V_{IR}), two voltage regions have emerged: one in the range of 0.8 V–0.4 V, which is having a shorter discharging duration and ascribed to EDLC, whereas, the other region (0.4 V downwards) with a much longer discharging duration is associated with the combination of EDLC and Faradaiccapacitances [50]. (*iii*) For Pa/WC*3*-t_4 composite, a larger IR drop is followed by a longer discharging region (0.4 V downwards), indicating lesser EDLC effect and larger combinatorial effect of EDLC and faradaic capacitance. (*iv*) Surprisingly, the IR drop for Pa/WC*3*-t_4 composite is larger than Pa/WC*1*-t_4 and Pa/WC*2*-t_4 composites, although the discharging time per attainable cell potential ($\Delta t/\Delta V$, where $\Delta V = V_{max} - V_{IR}$) is higher for Pa/WC*3*-t_4 (~3000 s/V) against Pa/WC*1*-t_4 and Pa/WC*2*-t_4 (~1800 and 2000 s/V, respectively), which leads to higher areal capacitance for Pa/WC*3*-t_4 with respect to Pa/WC*1*-t_4 and Pa/WC*2*-t_4 electrodes (shown later in Fig. 9e). This is because the galvanostatic charge/discharge for a given current density ($J = I/A$) is represented by Ref. [66]: $= \frac{J}{C}\Delta t + V_{IR}\ Or\ \Delta V = V - V_{IR} = \frac{J}{V}\Delta t\ OR\ C = J\frac{\Delta t}{\Delta V}$. Physically, this implies that even after a longer IR drop, the discharging duration is proportionally increased considerably due to the combinatorial effect to enhance the overall capacitive performance. EIS analysis (shown later) also corroborates this fact that the electrostatic series resistance (ESR) of Pa/WC*3*-t_4 is higher than that of Pa/WC*1*-t_4 and Pa/WC*2*-t_4, although the charge transfer resistance of Pa/WC*3*-t_4 is lesser (indicative of better capacitive performance) than that of the other counterparts (shown later in Fig. 11d). Generally, IR drop corresponds to the internal resistance of the electrode. For Pa/WC*3*-t_4 electrode, due to the high concentration of WCPs, charge transport properties are hindered due to electrostatic interaction with trapped charges at the WCPs to create a higher IR drop. But this larger IR drop is compensated by the higher combinatorial effect of EDLC and faradaic capacitance at higher WCP concentrations (to increase the discharge time considerably), leading to an overall increment in the supercapacitive performance of the Pa/WC*3*-t_4 electrode against others. Similar phenomenon is observed for other polymerization times too (*cf.* Fig. S11a-d, Supporting Information). Similar to CV results, in GCD case also, Pa/WC*1*-t_1 electrode depicts minimal capacitive characteristics due to low WCP concentration and low polymerization time.

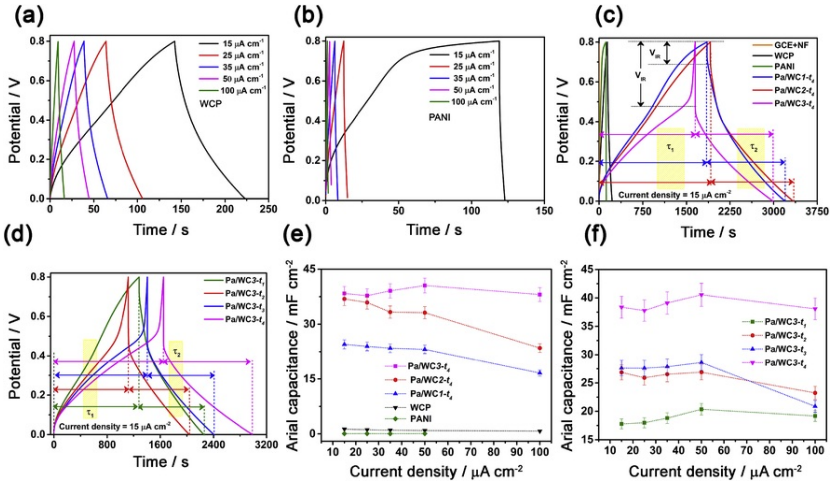

Fig. 9 GCD curves at different current densities for (a) waste carbon nanoparticles and (b) PANI. (c) Comparison of the GCD curves for three different composite samples at constant polymerization time t_4 = 3.0 h with control samples and GCE + NF electrode, (d) comparison of the GCD curves for Pa/WC*3* composite at four different polymerization times (t_1-t_4), (e) comparison of the areal capacitance as a function of current density for three different composite samples at constant polymerization time t_4 = 3.0 h with control samples, (f) comparison of the areal capacitance as a function of current density for Pa/WC*3* composite at four different polymerization times (t_1-t_4).

alt-text: Fig. 9

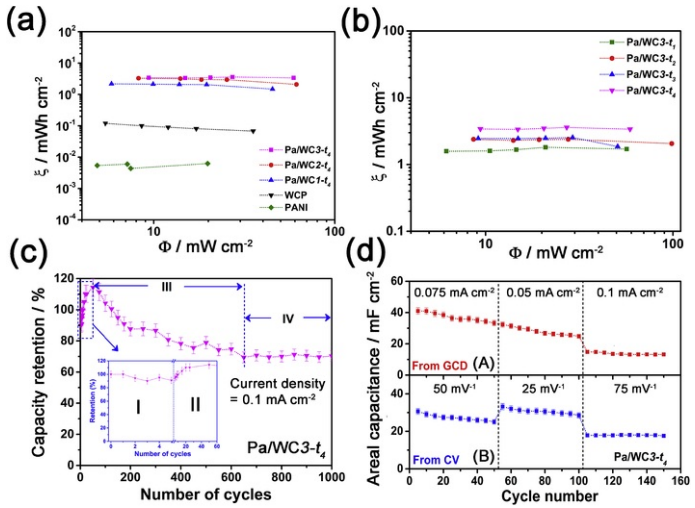

Fig. 10 Comparison of the Ragone plots for three different composite samples at constant polymerization time $t_4 = 3.0$ h with the control samples (a), and (b) Pa/WC*3* composite at four different polymerization times (t_1-t_4). Cyclic stability plots of Pa/WC3-t_4 composite sample over 1000 cycles (c), and (d) at progressively varied scan rates (A)/current densities (B). Inset of (c) is the cyclic stability for first 50 cycles. (d) Shows the cyclic performance at progressively varying scan rates (A) and current densities (B), respectively.

alt-text: Fig. 10

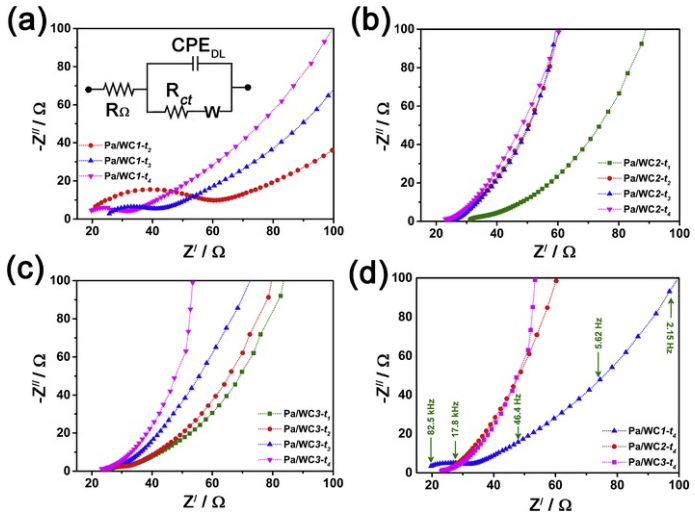

Fig. 11 Nyquist plots for composite electrodes, Pa/WC*1*-$t_2$to t_4 (a), Pa/WC*2*-t_1 to t_4 (b), Pa/WC*3*-t_1 to t_4, and (c) comparison of three composites Pa/WC*1* to *3*at t_4 (d). Inset of (a) represents the equivalent circuit.

alt-text: Fig. 11

As far as the effect of polymerization time on charge-discharge properties is concerned, Fig. 9d reveals that with the increase in polymerization time, charge-discharge curves are extended gradually, indicating improved capacitive performance, which is consistent with the CV data. And this trend is valid for all the samples with different WCP concentrations too (*cf.* Fig. S11e/f, Supporting Information). GCD curves of all samples with different WCP concentrations and different polymerization times are presented in a 2D-array in Fig. S10 (Supporting Information) for ready comparison. As can be seen from the figures, for a particular sample, the shapes of the curves are similar at different current densities, indicating stable GCD performance even at very high current densities. Also, the coulombic efficiency ($\eta\% = [\tau_2/\tau_1] \times 100$, where τ_2, τ_1 are discharging and charging times, respectively, *cf.* Fig. 9c) of the samples is found to be ranging from 75% (for Pa/WC*1*-t_4) to 80% (for Pa/WC*2*-t_4) to 90% (for Pa/WC*3*-t_4). As expected, higher WCP concentration increases the coulombic efficiency, indicating its very good applicability in practical devices. Again, with increasing polymerization time, the coulombic efficiency increases from 75% (for Pa/WC*3*-t_1) to

90% (for Pa/WC*3-t_4*) (*cf.* Fig. 9d). Similar trends are observed for other samples too.

The areal capacitance calculations from GCD curves, using Eqn. (2) are presented in Fig. 9e/f and for different WCP concentrations and polymerization times, respectively. As expected, the capacitance values for control samples (WCP and PANI) are very low, and enhanced considerably for composite electrodes. Also, with increase in WCP concentration and polymerization time, C-values increase considerably and in all cases, for a specific sample, the C-values remain near-constant (within 5%, as shown by the error bars) up to 50 μA cm^{-2}, and then deteriorate only 5% (for Pa/WC*3-t_4*) and ~30%–35% (for Pa/WC*1/2-t_4*) at a current density of 100 μA cm^{-2}. Similar trend is observed for all other samples with different WCP concentrations and polymerization times (*cf.* Fig. S12, Supporting Information). This good retention of capacitance values at higher currentdensities manifests the high rate capability of the electrode materials [67], which is also consistent with the CV results. The areal capacitance values of all the samples, calculated from GCD curves at different current densities, are tabulated in Table S2 (Supporting Information), which are comparable to that calculated from CV data (Table S1, Supporting Information). As expected, Pa/WC*3-t_4* composite (having highest WCP concentration of 4 wt% and longest polymerization time of 3 h) reveals best capacitance values (highlighted with red) against all other samples, which is consistent with the CV data.

As far as the supercapacitive performances of previously reported PANI-carbon nanomaterial composites (Table S3 in Supporting Information) are concerned, majority have used either porous carbon as the host matrix and PANI nanomaterials as the filler inside the pores, or graphene/CNT as the primary backbone, and PANI nanomaterials/thin films are immobilized within it to fabricate the composite electrochemical electrode [65,68–76]. And, the electrochemical performance of the composite is compared with the individual components (primary carbon host and PANI), which shows an increment of the specific/areal capacitance around 2 to 5 times over the individual components. Apparently, PANI imparts pseudocapacitive characteristics on the EDLC performance of the carbon nanomaterials to enhance the supercapacitive properties of the composite electrode. In some cases, a hybrid material, consists of an equivalent mixture of carbon nanomaterials and PANI nanostructures/thin films, is synthesized (instead of host-filler composite structure form) as electrochemical electrode to observe two to three times enhanced electrochemical performance over the individual components [18,50,77–79]. But there are very few reports where PANI is used as the host matrix and carbon-based materials (such as acetylene black, nanodiamond, carbon aerogel *etc.*) are embedded within it to fabricate a composite electrode for enhanced (1.5–3 times increment in the specific capacitance value over PANI) electrochemical performance [10,19,80]. Interestingly, there is no report (to best of the authors' knowledge) on the use of carbon nanoparticles (that too from waste carbon source) as filler into the PANI matrix to fabricate composite electrochemical electrode, as in the current case. It is believed that the use of carbon-based fillers within the PANI matrix tends to toughen the PANI skeleton, thereby minimizing the shrinkage of PANI backbone during large cycling and thus, enhance the durability. Especially, the existence of strong hydrogen bonds between the PANI and carbon-based fillers considerably affects the cycling stability of PANI-based composite electrodes [10]. In the current report, the WCP-incorporated PANI composite electrodes have revealed almost 2-3 orders of magnitude increment of the areal capacitance value (nearly 60 to 600 times increment) with respect to pure PANI electrode. Since the specific capacitance value is highly dependent on several factors (like fabrication process, mass loading, active area of the electrode, electrode configuration, sample resistance including electrolyte and or contact resistances, among others), therefore, to judge the performance of an composite electrochemical electrode against various literature values, it is scientifically reasonable to compare the relative increment of the C-values against the control sample in a particular report, rather than the absolute C-values of different reports. In that respect, in the current report, the enormous increment in the areal capacitance of the Pa/WC composite against pure PANI electrode clearly highlights the novelty of the current material and the method, and hence, warrants considerable attention.

The energy and power density are two key parameters for evolving the practical application of electrochemical electrode materials in supercapacitors. These parameters can be analyzed by the Ragone plot of areal energy density (ξ, in Wh cm^{-2}) versus power density (Φ, in W cm^{-2}) calculated from the GCD curves. But in this regard, it must also be mentioned that, usually the Ragone plots are studied for a packaged device rather than a half cell (or an electrochemical electrode). Though with the emergent field of developing new electrode materials in parallel with conventional materials with novel nanostructured morphologies, it is becoming more relevant to analyze the energy/power performance of individual components of the half cell (like electrode or electrolyte). This means, for new electrode material with novel properties, its application in a half-cell can be useful to isolate the energy/power performance individually to understand the effects of the changes to this component while avoiding the cost of developing a packaged device. As this in turn helps not only to determine or interpret the effects of individual component on the comprehensive electrochemical performances, but also to save resources required to develop a packaged device. Due to this reason, various groups are presenting the energy-power performance of half-cells with electrodes consists of novel materials [81], and we have also presented the same for our novel electroactive material. Therefore, Ragone plots of the samples are shown in Fig. 10a and b, using Eqns. 3 and 4 [82]. Fig. 10a depicts that the energy and power performances of the composite electrodes are higher than that of the control samples (WCP and PANI). Additionally, with increase in the WCP concentration (Fig. 10a) as well as the polymerization time (Fig. 10b) the energy/power performance is improved, which is consistent with CV and GCD data. Most importantly, the power density is increased almost one order of magnitude without compromising too much of energy density. For example, for Pa/WC*3-t_4* electrode, the power density is increased about 530% with a mere 1% decrement in the energy density. This depicts its potential superior applications in high-power devices.

Also, for practical applicability of an electroactive material in supercapacitors, high capacity retention over a large number of cycles (*i.e.* the long cycling life) is considered to be very important attribute itself. Fig. 10c shows the capacity retention graph for Pa/WC*3-t_4* sample over 1000 galvanostatic charge-discharge cycles for a constant 100 μA cm^{-2} current density. As shown in Fig. 10c and the inset, it consists of four regions. For the first 5 cycles (region I) the capacity values fluctuate (between 90 and 100%), which is showing a standard transient region, indicating the initiation of the charge trapping into the waste carbon nanoparticles within PANI matrix for the first few cycles. Beyond this, up to 60 cycles (region II), a steady increase in the capacity is observed (up to ~120% of the initial value). This is because, for the first 50–60 cycles, the charge trapping becomes more effective. This implies that during GCD measurement, when the potential is increased with time at a constant current density, some of the charges flowing through the electrolyte-active material-current collector system is being trapped into the WCP layer of the active material (as described in Fig. 8). As the system is current controlled, more charge flux is passed through the electrolyte-electrode interface to compensate over the lost charges during trapping. This further enhances the trapping and consequently increases the discharge time over the first 50–60 cycles, and hence, the capacity is increased gradually up to 60 cycles. Beyond this (region III), the charge trapping across the WCPs becomes near-saturated, and hence no further charge trapping occurs. But the trapped charges pose a repulsive force on the incoming charges passing through the electrolyte-active

material-current collector ternary system, manifesting increased resistivity of the electroactive material, which subsequently decreases the capacitance value (up to ~ 80% of the original value till 650 cycles, region III) and then a dynamic equilibrium is established, and the C-values become steady up to 1000 cycles (region IV). This considerably high capacity retention indicates excellent stability for high performance supercapacitors. To further verify the retention of high *C*-values at higher scan rates and larger current densities (as shown in Fig. 7e/f and 9e/f) in terms of cyclic stability, the cyclic performance is tested at progressively varying current densities (Fig. 10d-A) and scan rates (Fig. 10d-B), respectively. Interestingly it has been observed that, even when the electrochemical electrode is subjected to a sudden change in the scan rate/current density, the areal capacitance still remained highly stable at each scan rate/current density, and still retained very high value, even at the higher scan rate/current density. These results indicate that the Pa/WC composites meet the two important requirements of long cycling lifetime and good rate capability for potential applications in practical energy storage devices [55].

3.2.3 Electrochemical impedance spectroscopic measurements

Electrochemical impedance spectroscopic (EIS) measurements have been carried out to explore the kinetic properties of the electrodes. Fig. 11 depicts the Nyquist plots for as-prepared composites, from low-to-high frequency regions. All theplots consist of (*i*) a slightly depressed semicircle at the high-to-midfrequency regionsrepresenting the Warburg curve, which signifies a parallel combination of chargetransferresistance (R_{ct}) and a double-layer capacitance (CPE_{DL}). R_{ct}, which is equal to the diameter of the semicircle, basically is used to describe the redox reactionoccurring at the electrode-electrolyte interface. On the other side, CPE_{DL} characterizes the constant phase element (*CPE*) occurring at the solid–liquid interface because of the ionic/electronic charge separations. Moreover, CPE_{DL} is being used here (not the double layer capacitance i.e. C_{DL}), as the semicircles are distorted. (*ii*) an intercept on the real axis at high frequency, indicating the electrostatic series resistance (ESR, R_{Ω}) which combines the effects of electrolyte (ionic) resistance, internal resistance of electroactive material and the contact resistance at the solid-liquid interface and (*iii*) a linear part in the low frequency region representing the Warburg impedance (*W*). The ion-diffusion from electrolyte to electroactive material, and the insertion capacitance as an effect of charge-accumulation at the electrode surface are key factors in this connection. Warburg coefficient (ψ_w) is often used to predict *W* and diffusion coefficients. The near-vertical slope of this section demonstrates the ideal capacitive nature of the electrode, whereas the angle of about 45-60^{O} with the real axis signifies that the electrochemical process is either slightly diffusion controlled and/or is a result of frequency dispersion due to a wide size distribution/roughness variation within the active materials [19,30,79,83]. Fig. 11a depicts that at lower WCP concentration (Pa/WC*1*-$t_{2\text{-}4}$, with 1 wt% of WCP), the semicircular part is widened, indicating higher charge transfer resistance of the electrodes. With increase in the polymerization time, the diameter of the semicircle is decreased and the slope of the linear part is increased from ~45° to 60°, indicating a reduction in the charge-transfer resistance and a gradual transition from diffusion-controlled behavior to ideal capacitive behavior. For other samples also (Fig. 11b-c) the slope is increased with an increase in the polymerization time, indicating similar transition behavior of diffusion-controlled to ideal capacitive process. Especially, for Pa/WC*3*-t_4 (which revealed best capacitive performance through CV and GCD analyses shown earlier), near-vertical slope of the linear part of the Nyquist plot depicts excellent capacitive properties of this electrode. Additionally, at the high-frequency region of the samples (having higher WCP concentrations: Pa/WC*2/3*-$t_{1\text{-}4}$, Fig. 11b/c), very small (or almost insignificant) semicircular parts are observed, indicating negligible charge-transfer resistance, which is due to very low Faradaic resistances of the composite electrodes, thus confirming very good electrochemical properties. Similar insignificant semi-circular regions in the Nyquist plots have already been reported for graphene-PANI-based nanocomposite films and attributed to the low-Faradaic resistance of the films [50]. Also, in Fig. 11d, it has been observed that the high frequency intercept at the real axis is higher for Pa/WC*3*-t_4 composite against others, which is consistent with GCD curves where higher IR drop is observed for the sample having highest WCP concentration (*cf.* Fig. 9c). According to the shapes of the Nyquist plots, the EIS data are fitted with typical equivalent circuit [R_{Ω} + CPE_{DL} || (R_{ct} + *W*)] shown in the inset of Fig. 11a [19]. The fitted values are presented in Table 2, and the fitting is shown in Fig. S13 (Supplementary Information). The lines are the fitted curves with the experimental data (scatter plot). The error bar indicates the fitting is well-within the 5% of the experimental values. Expectedly, Pa/WC*3*-t_4 composite showed highest CPE_{DL} (36.4 μF) and lowest R_{ct} (2.52Ω) values against other samples, which indicate much easier charge transfer rate at the electrode/electrolyte interface, thus enhancing rate capability and cycle life towards achieving superior supercapacitor performance. The fitted EIS data are also consistent with the CV and GCD data, where Pa/WC*3*-t_4 showed highest areal capacitance against other samples, indicating highly stable and reproducible electrochemical properties of the samples.

Table 2 Fitted values of EIS data from the Nyquist plots.

alt-text: Table 2

EIS parameters	Pa/WC*1*-t_4	Pa/WC*2*-t_4	Pa/WC*3*-t_4
R_{Ω}/Ω	18.4	20.63	23.41
CPE_{DL}/μF	0.367	1.22	36.4
R_{ct}/Ω	19.19	3.12	2.52
Ψ_w/Ω $s^{-1/2}$	242.0	169.1	119.1

4 Conclusions

A high performance supercapacitor electrode material has been prepared by incorporating carbon nanoparticles into polyaniline matrix via a simple, cost-effective and environment-friendly wet-chemical route. It is worthwhile

to mention that the source of carbon in this work is normal cooking oven produced waste carbon material (kind of biomass or biowaste) which is natural and renewable. These particles are not chemically modified further; hence, no time-consuming or complex pre-treatments have been involved. Clearly, the preparation process of the WCP-PANI composites is therefore eco-friendly as well as cheaper and time-saving. The obtained composites combine the essential EDLC properties of the carbon source and pseudocapacitive behavior of PANI with enhanced synergetic effects. The incorporation of WCP in greater concentration significantly improves the charge-trapping phenomena within the active material thus formed. The electrochemical results show that the composite microelectrodes possess excellent capacitive behavior along with good rate capability and cyclic stability. For example, the composite electrodes depict almost 80% retention of the capacitance over 1000 cycles, and nearly 90–100% retention of C-values with increasing scan rates (from 10 to 100 $mV\,s^{-1}$) and current densities (from 10 to 100 $\mu A\,cm^{-2}$). Especially, the unique charge trapping capabilities of the composite electrodes manifest considerably improved areal capacitance at higher scan rates and current densities, indicating potential applications in high performance charge storage devices. Also, the areal capacitance of the composite electrode is found to increase significantly (more than 600 times) over pure PANI electrode and the energy-power performance of the microelectrode reveals almost 550% increment in the power density with a mere 1% decrement in energy density. These data are significantly higher than the reported values. Thus, as-produced composite electrode with low-cost, eco-friendly processing method, utilizing waste carbon particles as one of its major components, can contribute towards the development of promising and highly efficient supercapacitors using green nanotechnology for energy storage systems.

Acknowledgements

S. Goswami and S. Nandy acknowledge the funding from European Community H2020 program under grant agreement No. 685758 (project 1D-Neon). Also, this work was partially financed by FEDER funds through the COMPETE 2020 Programme and National Funds through FCT under the project UID/CTM/50025/2013. The authors want to give special thanks to Maria João Oliveira for Raman measurements, Prof. Daniela Nunes for FESEM measurements and Dr. Jonas Deuermeier for XPS measurement.

Appendix A. Supplementary data

Supplementary data to this article can be found online at https://doi.org/10.1016/j.electacta.2019.05.133.

References

[1] M.F. El-Kady, Y. Shao and R.B. Kaner, Graphene for batteries, supercapacitors and beyond, *Nat. Rev. Mater.* **1** (14pp), 2016, 16033.

[2] G. Qu, J. Cheng, X. Li, D. Yuan, P. Chen, X. Chen, B. Wang and H. Peng, A fiber supercapacitor with high energy density based on hollow graphene/conducting polymer fiber electrode, *Adv. Mater.* **28**, 2016, 3646–3652.

[3] Z. Wang, D.O. Carlsson, P. Tammela, K. Hua, P. Zhang, L. Nyholm and M. Strømme, Surface modified nanocellulose fibers yield conducting polymer-based flexible supercapacitors with enhanced capacitances, *ACS Nano* **9**, 2015, 7563–7571.

[4] A. González, E. Goikolea, J.A. Barrena and R. Mysyk, Review on supercapacitors: technologies and materials, *Renew. Sustain. Energy Rev.* **58**, 2016, 1189–1206.

[5] B.E. Conway, Electrochemical Supercapacitors: Scientific Fundamentals and Technological Applications, 1999, Kluwer; New York.

[6] A. Nishino, Capacitors: operating principles, current market and technical trends, *J. Power Sources* **60**, 1996, 137–147.

[7] J.R. Miller and P. Simon, Electrochemical capacitors for energy management, *Science* **321**, 2008, 651–652.

[8] P. Simon and Y. Gogotsi, Materials for electrochemical capacitors, *Nat. Mater.* **7**, 2008, 845–854.

[9] M. Mastragostino, F. Soavi and C. Arbizzani, Electrochemical supercapacitors, In: W. van Schalkwijk and B. Scrosati, (Eds.), *Advances in Lithium-Ion Batteries,* 2002, Springer; Boston, MA, 481–505.

[10] I. Kovalenko, D.G. Bucknall and G. Yushin, Detonation nanodiamond and onion-like-carbon-embedded polyaniline for supercapacitors, *Adv. Funct. Mater.* **20**, 2010, 3979–3986.

[11] C. Falco, M. Sevilla, R.J. White, R. Rothe and M.M. Titirici, Renewable nitrogen-doped hydrothermal carbons derived from microalgae, *Chem. Sus. Chem.* **5**, 2012, 1834–1840.

[12] L. Zhao, L.Z. Fan, M.Q. Zhou, H. Guan, S. Qiao, M. Antonietti, et al., Nitrogen-containing hydrothermal carbons with superior performance in supercapacitors, *Adv. Mater.* **22**, 2010, 5202–5206.

[13] L. Su, F. Gao and L. Mao, Electrochemical properties of carbon nanotube (CNT) film electrodes prepared by controllable adsorption of CNTs onto an alkanethiol monolayer self-assembled on gold electrodes, *Anal. Chem.* **78**, 2006, 2651–2657.

[14] Y.H. Gwon, J.K. Ha, K.K. Cho and H.S. Kim, Physical and electrochemical properties of synthesized carbon nanotubes [CNTs] on a metal substrate by thermal chemical vapor deposition, *Nanoscale Res. Lett.* **7** (5pp), 2012, 61.

[15] J. Yan, T. Wei, B. Shao, F. Ma, Z. Fan, M. Zhang, C. Zheng, Y. Shang, W. Qian and F. Wei, Electrochemical properties of graphene nanosheet/carbon black composites as electrodes for supercapacitors, *Carbon* **48**, 2010, 1731–1737.

[16] G.A. Snook, P. Kao and A.S. Best, Conducting-polymer-based supercapacitor devices and electrodes, *J. Power Sources* **196**, 2011, 1–12.

[17] A. Eftekhari, L. Li and Y. Yang, Polyaniline supercapacitors, *J. Power Sources* **347**, 2017, 86–107.

[18] Z. Lei, Z. Chen and X.S. Zhao, Growth of polyaniline on hollow carbon spheres for enhancing electrocapacitance, *J. Phys. Chem.* **C114**, 2010, 19867–19874.

[19] S. Goswami, S. Nandy, J. Deuermeier, A.C. Marques, D. Nunes, S.P. Patole, P.M.F.J. Costa, R. Martins and E. Fortunato, Green nanotechnology from waste carbon–polyaniline composite: generation of wavelength-independent multiband photoluminescence for sensitive ion detection, *Adv. Sust. Sys.* **2** (11pp), 2018, 1700137.

[20] S. BalSydulu, S. Palaniappan and P. Srinivas, Nano fibre polyaniline containing long chain and small molecule dopants and carbon composites for supercapacitor, *Electrochim. Acta* **95**, 2013, 251–259.

[21] C. Zhan, X. Yu, Q. Liang, W. Liu, Y. Wang, R. Lv, Z.-H. Huang and F. Kang, Flour food waste derived activated carbon for high-performance supercapacitors, *RSC Adv.* **6**, 2016, 89391–89396.

[22] P. Cheng, T. Li, H. Yu, L. Zhi, Z. Liu and Z. Lei, Biomass-derived carbon fiber aerogel as a binder-free electrode for high-rate supercapacitors, *J. Phys. Chem.* **C120**, 2016, 2079–2086.

[23] W. Qian, F. Sun, Y. Xu, L. Qiu, C. Liu, S. Wang and F. Yan, Human hair-derived carbon flakes for electrochemical supercapacitors, *Energy Environ. Sci.* **7**, 2014, 379–386.

[24] G. Inal, II, S.M. Holmes, A. Banford and Z. Aktas, The performance of supercapacitor electrodes developed from chemically activated carbon produced from waste tea, *Appl. Surf. Sci.* **357**, 2015, 696–703.

[25] X. Gu, Y. Wang, C. Lai, J. Qiu, S. Li, Y. Hou, W. Martens, N. Mahmood and S. Zhang, Microporous bamboo biochar for lithium-sulfur batteries, *Nano Res.* **8**, 2015, 129–139.

[26] S. Goswami, S. Nandy, A.N. Banerjee, A. Kiazadeh, G.R. Dillip, J.V. Pinto, S.W. Joo, R. Martins and E. Fortunato, “Electro-Typing” on a carbon-nanoparticles-filled polymeric film using conducting atomic force microscopy, *Adv. Mater.* **29** (9pp), 2017, 1703079.

[27] K. Paritosh, S.K. Kushwaha, M. Yadav, N. Pareek, A. Chawade and V. Vivekanand, Food waste to energy: an overview of sustainable approaches for food waste management and nutrient recycling, *BioMed Res. Int.* **2017**, 2017, 19, Article ID 2370927.

[28] A.F. Carvalho, A.J.S. Fernandes, C. Leitão, J. Deuermeier, A.C. Marques, R. Martins, E. Fortunato and F.M. Costa, Laser-induced graphene strain sensors produced by ultraviolet irradiation of polyimide, *Adv. Funct. Mater.* **28**, 2018, 1805271.

[29] M. Zhen, S. Guo, G. Gao, Z. Zhou and L. Liu, TiO_2–B nanorods on reduced graphene oxide as anode materials for Li ion batteries, *Chem. Commun.* **51**, 2015, 507–510.

[30] M. Ates, Review study of electrochemical impedance spectroscopy and equivalent electrical circuits of conducting polymers on carbon surfaces, *Prog. Org. Coating* **71**, 2011, 1–10.

[31] S.Z. Mortazavi, P. Parvin, A. Reyhani, S. Mirershadi and R.S. Bonabi, Generation of various carbon nanostructures in water using IR/UV laser ablation, *Phys. D: Appl. Phys.* **46**, 2013, 165303.

[32] A.J. Roberts and C.E. Moffitt, Trends in XPS instrumentation for industrial surface analysis and materials characterisation, *J. Electron. Spectrosc. Relat. Phenom.* **231**, 2019, 68–74.

[33] J. Yang, J. Kim, J. Lee, S. Min, H. Kim, K.L. Wang and J. Hong, Electrostatic force microscopy measurements of charge trapping behavior of Au nanoparticles embedded in metal-insulator-semiconductor structure, *Ultramicroscopy* **108**, 2008, 1215–1219.

[34] P. Girard, Electrostatic force microscopy: principles and some applications to semiconductors, *Nanotechnology* **12**, 2001, 485–490.

[35] A. Lodha, S.M. Kilbey, P.C. Ramamurthy and R.V. Gregory, Effect of annealing on electrical conductivity and morphology of polyaniline films, *J. Appl. Polym. Sci.* **82**, 2001, 3602–3610.

[36] W.A.K. Mahmood and M.H. Azarian, Sol-gel synthesis of polyaniline/zirconia composite conducting materials, *J. Polym. Res.* **23** (8pp), 2016, 88.

[37] G. Gheno, N.R.S. Basso and R. Hubler, Polyaniline/Graphite nanocomposites: synthesis and characterization, *Macromol. Symp.* **299/300**, 2011, 74–80.

[38] G. Bar, Y. Thomann, R. Brandsch, H.J. Cantow and M.H. Whangbo, Factors affecting the height and phase images in tapping mode atomic force microscopy. Study of phase-separated polymer blends of poly(ethene-co-styrene) and poly(2,6-dimethyl-1,4-phenylene oxide), *Langmuir* **13**, 1997, 3807–3812.

[39] S. Nandy, G. Gonçalves, J.V. Pinto, T. Busani, V. Figueiredo, L. Pereira, R. Martins and E. Fortunato, Current transport mechanism at metal–semiconductor nanoscale interfaces based on ultrahigh density arrays of p-type NiO nano-pillars, *Nanoscale* **5**, 2013, 11699–11709.

[40] A. Leon, B.J. Rodier, Q. Luo, C.M. Hemmingsen, P. Wei, K. Abbasi, R. Advincula and E.B. Pentzer, Distinct chemical and physical properties of janus nanosheets, *ACS Nano* **11**, 2017, 7485–7493.

[41] M. Aymen, S. Sami, S. Ahmed, G. Fethi and B.M. Abdellatif, Correlation between Raman spectroscopy and electrical conductivity of graphite/polyaniline composites reacted with hydrogen peroxide, *J. Phys. D Appl. Phys.* **46** (6pp), 2013, 335103.

[42] G.M. do Nascimento and M.L.A. Temperini, Studies on the resonance Raman spectra of polyaniline obtained with near-IR excitation, *J. Raman Spectrosc.* **39**, 2008, 772–778.

[43] L. Li, Z.Y. Qin, X. Liang, Q.Q. Fan, Y.Q. Lu, W.H. Wu and M.-F. Zhu, Facile fabrication of uniform Core−Shell structured carbon Nanotube−Polyaniline nanocomposites, *J. Phys. Chem.* **C113**, 2009, 5502–5507.

[44] N.A. Ogurtsov, Y.V. Noskov, V.N. Bliznyuk, V.G. Ilyin, J.L. Wojkiewicz, E.A. Fedorenko and A.A. Pud, Evolution and interdependence of structure and properties of nanocomposites of multiwall carbon nanotubes with polyaniline, *J. Phys. Chem.* **C120**, 2016, 230–242.

[45] S.Y. Park, H.U. Lee, E.S. Park, S.C. Lee, J.W. Lee, S.W. Jeong, C.H. Kim|, Y.-C. Lee, Y.S. Huh and J. Lee, Photoluminescent green carbon nanodots from food-waste-derived sources: large-scale synthesis, properties, and biomedical applications, *ACS Appl. Mater. Interfaces* **6**, 2014, 3365–3370.

[46] S. Nandy, R. Thapa, M. Kumar, T. Som, N. Bundaleski, O.M.N.D. Teodoro, R. Martins and E. Fortunato, Efficient field emission from vertically aligned $Cu_2O_{1-\delta}$(111) nanostructure influenced by oxygen vacancy, *Adv. Funct. Mater.* **25**, 2015, 947–956.

[47] D. Nunes, T.R. Calmeiro, S. Nandy, J.V. Pinto, A. Pimentel, P. Barquinha, P.A. Carvalho, J.C. Walmsley, E. Fortunato and R. Martins, Charging effects and surface potential variations of Cu-based nanowires, *Thin Solid Films* **601**, 2016, 45–53.

[48] C. Musumeci, A. Liscio, V. Palermo and P. Samorı`, Electronic characterization of supramolecular materials at the nanoscale by conductive atomic force and Kelvin probe force microscopies, *Mater. Today* **17**, 2014, 504–517.

[49] B. Li, X. Li, J. Zai and X. Qian, Facile synthesis of porous Zn-Sn-O nanocubes and their electrochemical performances, *Nano-Micro Lett.* **8** (2), 2016, 174–181.

[50] Q. Wu, Y. Xu, Z. Yao, A. Liu and G. Shi, Supercapacitors based on flexible graphene/polyaniline nanofiber composite films, *ACS Nano* **4**, 2010, 1963–1970.

[51] H.W. Park, T. Kim, J. Huh, M. Kang, J.E. Lee and H. Yoon, Anisotropic growth control of polyaniline nanostructures and their morphology-dependent electrochemical characteristics, *ACS Nano* **6**, 2012, 7624–7633.

[52] E. Lust, G. Nurk, A. Janes, M. Arulepp, L. Permann, P. Nigu and P. Moller, Electrochemical properties of nanoporous carbon electrodes, Cond, *Matter Phys.* **5**, 2002, 307–327.

[53] G.R. Dillip, A.N. Banerjee, V.C. Anitha, B.D.P. Raju, S.W. Joo and B.K. Min, Oxygen vacancy-induced structural, optical, and enhanced supercapacitive performance of zinc oxide anchored graphitic carbon nanofiber hybrid electrodes, *ACS Appl. Mater. Interfaces* **8**, 2016, 5025–5039.

[54] C. Tran, R. Singhal, D. Lawrence and V. Kalra, Polyaniline-coated freestanding porous carbon nanofiber as efficient hybrid electrodes for supercapacitors, *J. Power Sources* **293**, 2015, 373–379.

[55] Z.L. Wang, X.J. He, S.H. Ye, Y.X. Tong and G.R. Li, Design of polypyrrole/polyaniline double-walled nanotube Arrays for electrochemical energy storage, *ACS Appl. Mater. Interfaces* **6**, 2014, 642–647.

[56] A.N. Banerjee, V.C. Anitha and S.W. Joo, Improved electrochemical properties of morphology-controlled titania/titanate nanostructures prepared by in-situ hydrothermal surface modification of self-source Ti substrate for high-performance supercapacitors, *Sci. Rep.* **7** (20pp), 2017, 13227.

[57] X. Lang, A. Hirata, T. Fujita and M. Chen, Nanoporous metal/oxide hybrid electrodes for electrochemical supercapacitors, *Nat. Nanotechnol.* **6**, 2011, 232–236.

[58] H. Wang and L. Pilon, Physical interpretation of cyclic voltammetry for measuring electric double layer capacitances, *Electrochim. Acta* **64**, 2012, 130–139.

[59] H. Wang, A. Thiele and L. Pilon, Simulations of cyclic voltammetry for electric double layers in asymmetric electrolytes: a generalized modified Poisson–Nernst–Planck model, *J. Phys. Chem. C* **117**, 2013, 18286–18297.

[60] R. Nurzulaikha, H.N. Limb, I. Harrison, S.S. Lim, A. Pandikumar, N.M. Huang, S.P. Lim, G.S.H. Thien, N. Yusoff and I. Ibrahim, Graphene/SnO_2 nanocomposite-modified electrode for electrochemical detection of dopamine, *Sens. Biosensing Res.* **5**, 2015, 42–49.

[61] Q. Xu, S.X. Gu, L. Jin, Y.E. Zhou, Z. Yang, W. Wang and X. Hu, Graphene/polyaniline/gold nanoparticles nanocomposite for the direct electron transfer of glucose oxidase and glucose biosensing, *Sensor. Actuator. B Chem.* **190**, 2014, 562–569.

[62] D. Shan, J. Zhang, H.G. Xue, S.N. Ding and S. Cosnier, Colloidal laponite nanoparticles: extended application in direct electrochemistry of glucose oxidase and reagentless glucose biosensing, *Biosens. Bioelectron.* **25**, 2010, 1427–1433.

[63] A.G.M. Ferrari, C.W. Foster, P.J. Kelly, D.A.C. Brownson and C.E. Banks, Determination of electrochemical area of screen-printed electrochemical sensing platforms, *Biosensors* **8** (2), 2018, 53, (10pp).

[64] M. Salari, S.H. Aboutalebi, A.T. Chidembo, I.P. Nevirkovets, K. Konstantinov and H.K. Liu, Enhancement of the electrochemical capacitance of TiO_2 nanotube arrays through controlled phase transformation of anatase to rutile, *Phys. Chem. Chem. Phys.* **14**, 2012, 4770–4779.

[65] Y. Li, X. Zhao, P. Yu and Q. Zhang, Oriented arrays of polyaniline nanorods grown on graphite nanosheets for an electrochemical supercapacitor, *Langmuir* **29**, 2013, 493–500.

[66] J. Ma, New Electrochemical Characterization Methods for Nanocomposite Supercapacitor Electrodes, arXiv:1406.0470v3 [cond-mat.mtrl-sci] 19 Apr 2016 (7pp).

[67] Jaidev, R.I. Jafri, A.K. Mishra and S. Ramaprabhu, Polyaniline–MnO_2 nanotube hybrid nanocomposite as supercapacitor electrode material in acidic electrolyte, *J. Mater. Chem.* **21**, 2011, 17601–17605.

[68] H. Wang, J. Lin and Z.X. Shen, Polyaniline (PANi) based electrode materials for energy storage and conversion, *J. Sci. Adv. Mater. Dev.* **1**, 2016, 225–255.

[69] Y.G. Wang, H.Q. Li and Y.Y. Xia, Ordered whisker like polyaniline grown on the surface of mesoporous carbon and its electrochemical capacitance performance, *Adv. Mater.* **18**, 2006, 2619–2623.

[70] W. Fan, Y.E. Miao, L. Zhang, Y. Huang and T. Liu, Porous graphene–carbon nanotube hybrid paper as a flexible nano-scaffold for polyaniline immobilization and application in all-solid-state supercapacitors, *RSC Adv.* **5** 2015, 31064–31073.

[71] J. Li, Y. Ren, Z. Ren, S. Wang, Y. Qiu and J. Yu, Aligned polyaniline nanowires grown on the internal surface of macroporous carbon for supercapacitors, *J. Mater. Chem.* **A3**, 2015, 23307–23315.

[72] N. Hu, L. Zhang, C. Yang, J. Zhao, Z. Yang, H. Wei, H. Liao, Z. Feng, A. Fisher, Y. Zhang and Z.J. Xu, Three-dimensional skeleton networks of graphene wrapped polyaniline nanofibers: an excellent structure for high-performance flexible solid-state supercapacitors, *Sci. Rep.* **6** (10pp), 2016, 19777.

[73] S. Zeng, H. Chen, F. Cai, Y. Kang, M. Chen and Q. Li, Electrochemical fabrication of carbon nanotube/polyaniline hydrogel film for all-solid-state flexible supercapacitor with high areal capacitance, *J. Mater. Chem. A* **3**, 2015, 23864–23870.

[74] M. Hao, Y. Chen, W. Xiong, L. Zhang, L. Wu, Y. Fu, T. Mei, J. Wang, J. Li and X. Wan, Coherent polyaniline/graphene oxides/multi-walled carbon nanotubes ternary composites for asymmetric supercapacitors, *Electrochim Acta* **191**, 2016, 165–172.

[75] C. Peng, S. Zhang, D. Jewell and G.Z. Chen, Carbon nanotube and conducting polymer composites for supercapacitors, *Prog. Nat. Sci.* **18**, 2008, 777–788.

[76] Z. Lei, X. Sun, H. Wang, Z. Liu and X.S. Zhao, Platelet CMK-5 as an excellent mesoporous carbon to enhance the pseudocapacitance of polyaniline, *ACS Appl. Mater. Interfaces* **5**, 2013, 7501–7508.

[77] Md N. Hyder, S.W. Lee, F.Ç. Cebeci, D.J. Schmidt, H.-Y. Shao and P.T. Hammond, Layer-by-Layer assembled polyaniline nanofiber/multiwall carbon nanotube thin film electrodes for high-power and high-energy storage

applications, *ACS Nano* **5**, 2011, 8552–8561.

[78] H. Wang, F. Presuel and R.G. Kelly, Computational modeling of inhibitor release and transport from multifunctional organic coatings, *Electrochim. Acta* **49**, 2004, 239–255.

[79] B. Dong, B.L. He, C.L. Xu and H.L. Li, Preparation and electrochemical characterization of polyaniline/multi-walled carbon nanotubes composites for supercapacitor, *Mater. Sci. Eng. B* **143**, 2007, 7–13.

[80] F. Xu, G. Zheng, D. Wu, Y. Liang, Z. Li and R. Fu, Improving electrochemical performance of polyaniline by introducing carbon aerogel as filler, *Phys. Chem. Chem. Phys.* **12**, 2010, 3270–3275.

[81] L. Mai, H. Li, Y. Zhao, L. Xu, X. Xu, Y. Luo, Z. Zhang, W. Ke, C. Niu and Q. Zhang, Fast ionic diffusion-enabled nanoflake electrode by spontaneous electrochemical pre-intercalation for high-performance supercapacitor, *Sci. Rep.* **3** (8pp), 2013, 1718.

[82] T. Li, Y. Wu, Q. Wang, D. Zhang, A. Zhang and M. Miao, TiO_2 crystalline structure and electrochemical performance in two-ply yarn CNT/TiO_2 asymmetric supercapacitors, *J. Mater. Sci.* **52**, 2017, 7733–7743.

[83] Y.K. Zhou, B.L. He, W.J. Zhou, J. Huang, X.H. Li, B. Wu and H.-L. Li, Electrochemical capacitance of well-coated single-walled carbon nanotube with polyaniline composites, *Electrochim. Acta* **49**, 2004, 257–262.

Appendix A. Supplementary data

The following is the Supplementary data to this article:

Multimedia Component 1

Multimedia component 1

alt-text: Multimedia component 1

Graphical abstract

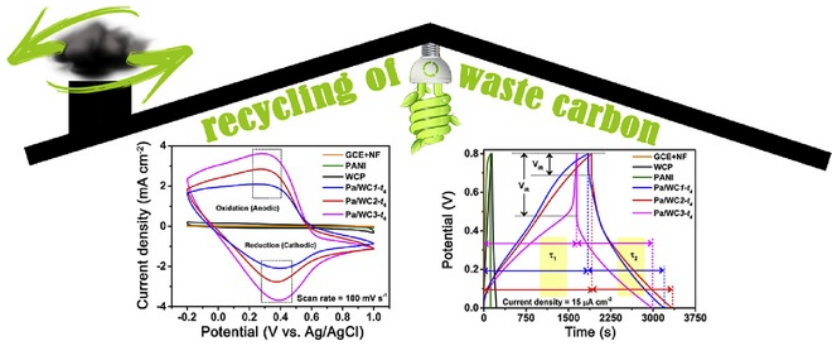

alt-text: Image 1

Highlights

- **Low cost sustainable economy:** With burgeoning interest in waste management systems, “reduce, reuse and recycle” of waste carbons are main three basic building factors for this scientific report. Which supports the development of next generation green-supercapacitors.
- **A novel charge-trapping phenomenon of PANI-WCP composites:** Due to which the diffusion limitations at the higher scan-rate/current-densities have been suppressed. This leads to an unusual increment in the areal capacitance of the PANI-WCP composite electrochemical electrode at higher scan-rate/current densities, the reason of which is explained for the first time (to best of authors' knowledge) by a physico-chemical model.

- **Huge increment of energy power efficiency:** composite electrode reveals almost 550% increment in the power density with a mere 1% decrement in energy density.

Queries and Answers

Query: Please confirm that the provided emails “s.nandy@fct.unl.pt/snandy_ju, arghya@ynu.ac.kr, emf@fct.unl.pt” are the correct address for official communication, else provide an alternate e-mail address to replace the existing one, because private e-mail addresses should not be used in articles as the address for communication.
Answer: All are correct.

Query: Have we correctly interpreted the following funding source(s) and country names you cited in your article: FCT, Portugal; FEDER; European Community H2020?
Answer: Yes

Query: Highlights should only consist of “125” characters per bullet point, including spaces. The highlights provided are too long; please edit them to meet the requirement.
Answer:
Attachments: Highlights.docx

Query: Please confirm that given names and surnames have been identified correctly and are presented in the desired order and please carefully verify the spelling of all authors’ names.
Answer: Yes

Query: Your article is registered as a regular item and is being processed for inclusion in a regular issue of the journal. If this is NOT correct and your article belongs to a Special Issue/Collection please contact a.elumalai@elsevier.com immediately prior to returning your corrections.
Answer: Yes